JGR Solid Earth

RESEARCH ARTICLE
10.1029/2020JB021302

Natural and Experimental Constraints on a Flow Law for Dislocation-Dominated Creep in Wet Quartz

Alexander D. J. Lusk[1,2], John P. Platt[2], and Jason A. Platt[3]

[1]Department of Geoscience, University of Wisconsin-Madison, Madison, WI, USA, [2]Department of Earth Sciences, University of Southern California, Los Angeles, CA, USA, [3]Department of Physics, University of California San Diego, La Jolla, CA, USA

Key Points:

- We use Bayesian statistical analysis on compiled rock deformation data to produce a flow law for dislocation creep in wet quartz
- This analysis indicates a low sensitivity to water fugacity, while other parameters are broadly consistent with existing values
- Under geological conditions, wet quartz aggregates deform faster than is predicted by existing flow laws

Supporting Information:

Supporting Information may be found in the online version of this article.

Correspondence to:

A. D. J. Lusk,
alusk@wisc.edu

Citation:

Lusk, A. D. J., Platt, J. P., & Platt, J. A. (2021). Natural and experimental constraints on a flow law for dislocation-dominated creep in wet quartz. *Journal of Geophysical Research: Solid Earth*, *126*, e2020JB021302. https://doi.org/10.1029/2020JB021302

Received 11 NOV 2020
Accepted 7 APR 2021

Abstract

We present a flow law for dislocation-dominated creep in wet quartz derived from compiled experimental and field-based rheological data. By integrating the field-based data, including independently calculated strain rates, deformation temperatures, pressures, and differential stresses, we add constraints for dislocation-dominated creep at conditions unattainable in quartz deformation experiments. A Markov Chain Monte Carlo (MCMC) statistical analysis computes internally consistent parameters for the generalized flow law: $\dot{\varepsilon} = A\sigma^n f_{H_2O}^r e^{-(Q+VP)/RT}$. From this initial analysis, we identify different *effective* stress exponents for quartz deformed at confining pressures above and below ~700 MPa. To minimize the possible effect of confining pressure, compiled data are separated into "low-pressure" (<560 MPa) and "high-pressure" (700–1,600 MPa) groups and reanalyzed using the MCMC approach. The "low-pressure" data set, which is most applicable at midcrustal to lower-crustal confining pressures, yields the following parameters: $\log(A) = -9.30 \pm 0.66$ MPa^{-n-r} s^{-1}; $n = 3.5 \pm 0.2$; $r = 0.49 \pm 0.13$; $Q = 118 \pm 5$ kJ mol^{-1}; and $V = 2.59 \pm 2.45$ cm^3 mol^{-1}. The "high-pressure" data set produces a different set of parameters: $\log(A) = -7.90 \pm 0.34$ MPa^{-n-r} s^{-1}; $n = 2.0 \pm 0.1$; $r = 0.49 \pm 0.13$; $Q = 77 \pm 8$ kJ mol^{-1}; and $V = 2.59 \pm 2.45$ cm^3 mol^{-1}. Predicted quartz rheology is compared to other flow laws for dislocation creep; the calibrations presented in this study predict faster strain rates under geological conditions by more than 1 order of magnitude. The change in n at high confining pressure may result from an increase in the activity of grain size sensitive creep.

Plain Language Summary

At conditions present in the middle and lower crust, rocks generally deform by ductile processes, instead of brittle fracture which is dominant closer to the Earth's surface. As a volumetrically dominant mineral in many crustal rocks, quartz is commonly thought to control the overall strength of the crust. Much of our understanding of how quartz behaves comes from deformation experiments; but to produce the same type of deformation we observe in middle- or lower-crustal rocks, experiments must be performed at conditions different from what natural rocks experience. The difference poses a potential issue in extrapolating experimental results to natural conditions. Here, we integrate mechanical data from deformation experiments and naturally deformed rocks to arrive at a quantitative relationship that relates material properties and deformation conditions to the rate at which quartz deforms. Because we add constraints at deformation conditions not attainable in experiments, we likely produce a more accurate representation of ductile quartz behavior. Our results indicate that quartz-rich rocks in the middle and lower crust deform at least an order of magnitude faster than previous predictions, which has important implications for crustal strength, geodynamic modeling, and potentially for the loading of seismically active faults.

1. Introduction

Constitutive relationships (i.e., flow laws) relate strain rate ($\dot{\varepsilon}$) to differential stress (σ), temperature (T), pressure (P), water fugacity (f_{H_2O}), and material properties for a given deformation mechanism. As one of the most abundant minerals in the crust, quartz is thought to control crustal rheology and is commonly used to model and predict the viscous behavior of the middle and lower crust (e.g., Brace & Kohlstedt, 1980; Hirth et al., 2001). At these depths, quartz deforms by dislocation creep, a thermally activated process that is driven by the nucleation, buildup, and motion of dislocations, resulting in viscous flow. Dislocation creep

follows a power law relationship between stress and strain rate and is temperature dependent, resulting in an exponential decrease of strength with increasing temperature.

Our understanding of quartz rheology relies on a preponderance of experimental studies. Because of the long time scales over which natural rock deformation occurs, experiments must be conducted at strain rates that are orders of magnitude faster than natural processes to activate the same deformation mechanism(s) observed in nature. For example, to achieve deformation dominated by crystal plastic processes (e.g., dislocation creep) at these high strain rates, experimental temperatures and stresses must be much higher than under geological conditions. Due to this scaling, small changes in flow law parameters can lead to significant variability in the predicted strain rate or viscosity when extrapolated to geological conditions (Boutonnet et al., 2013; Hirth et al., 2001; Lusk & Platt, 2020; Paterson, 1987; Tokle et al., 2019). Validation of flow law parameters is therefore required to determine if, and how well, experimental results can be extrapolated to natural rock deformation (Paterson, 1987; Paterson & Luan, 1990).

In an attempt to address this problem, pioneering work by Hirth et al. (2001) produced a "naturally constrained" flow law for dislocation creep in quartz by integrating data from rock deformation experiments with field-based constraints from the Ruby Gap Duplex (RGD) in central Australia. Using an assumed value for the stress exponent, based on experimental work of Gleason and Tullis (1995) and Luan and Paterson (1992), they incorporated field-based data to constrain other parameters. Since then, several additional studies have calculated strain rates and deformation conditions directly from the rock record, potentially providing further constraints (Behr & Platt, 2011; Hughes et al., 2020; Kidder et al., 2012; Lusk & Platt, 2020; Sassier et al., 2009; Stipp et al., 2002). Given the increase in available experimental and field-based data as well as advances in our understanding of thermobarometry and grain size evolution in strained rocks, a reevaluation of quartz dislocation creep flow law parameters is warranted.

Here, we use Bayesian statistical analysis on a data set comprising natural and experimental rock deformation data to calibrate a flow law for wet quartz in which the dominant deformation mechanism is dislocation creep. Our calibrated values for the stress exponent (n), activation energy (Q), activation volume (V), water fugacity exponent (r), and prefactor (A) are compared to other published flow laws and used to further investigate the potential effects of confining pressure and activation of multiple deformation mechanisms.

1.1. Anatomy of a Flow Law

Flow laws for quartz deforming by dislocation creep take the following generalized power law form:

$$\dot{\varepsilon} = A\sigma^n d^m f_{H_2O}^r e^{\left(-H/RT\right)} \tag{1}$$

where A is a constant prefactor, σ is differential stress, n is the stress exponent, d is the grain size, with exponent m, f_{H_2O} is the water fugacity, with exponent r, R is the universal gas constant, and T is temperature in degrees K. Dislocation creep is not sensitive to grain size, so $m = 0$. H is the activation enthalpy which can be expressed:

$$H = Q + VP \tag{2}$$

where Q is the activation energy, V is the activation volume, and P is the confining pressure. Significant variability exists in published values for the parameters listed above, examples of which are compiled in Table 1.

For steady-state dislocation creep with recovery by dislocation climb, a theoretical value of the stress exponent (n) calculated from Orowan's transport equation yields n in the range of 3–5, where the variability largely depends on the chosen model for dislocation multiplication and annihilation (Karato, 2008; Poirier, 1985). A generally accepted value for a climb-controlled subgrain-boundary recovery model is $n = 3$ (Karato, 2008). However, experimental studies commonly report a value of $n = 4$ (Table 1), and this value is commonly assumed in studies that do not independently calculate n (e.g., Chernak et al., 2009; Hirth et al., 2001; Holyoke & Kronenberg, 2013; Lu & Jiang, 2019). Some experimental data sets have been subsequently reinterpreted to arrive at parameter values that differ from the original published work. For example,

Journal of Geophysical Research: Solid Earth

10.1029/2020JB021302

Table 1
Previously Determined Flow Law Parameters Compiled From the Literature

Source	Calibration type	Deformation mechanism	Strain geometry	Deformation apparatus	Prefactor A (MPa^{-n} s^{-1})	Activation enthalpy H (kJ mol^{-1})	Activation volume V (cm^3 mol^{-1})	Stress exponent n	Grain size exponent m	Water fugacity exponent r
Kronenberg & Tullis (1984)	Experimental (as-is)	Dislocation creep ± GSS[a] creep	Axial compression	Solid medium	–	120–150	–	~2.9–3.2	0.18	–
	Experimental (0.4 wt.% water added)				–	170–220	–	~2.5–2.7	0.18	–
Paterson & Luan (1990)	Experimental	Dislocation creep	Axial compression	Gas	6.5×10^{-8}	135	–	3	–	–
Luan & Paterson (1992)	Experimental	Dislocation creep ± GSS[a] creep	Axial compression	Gas	4.0×10^{-10}	152 ± 71	–	4 ± 0.8	–	–
Gleason & Tullis (1995)	Experimental	Dislocation creep	Axial compression	Solid medium	1.1×10^{-4}	223 ± 56	–	4 ± 0.9	–	–
Rutter & Brodie (2004)	Experimental	Dislocation creep ± GSS[a] creep	Axial compression	Gas	1.2×10^{-5}	242 ± 24	–	2.97 ± 0.29	–	1
Fukuda et al. (2018)	Experimental: low T (600–750°C)	Dislocation creep	Axial compression	Solid medium	–	129 ± 33	–	2.9–5.2	–	1.0 ± 0.2
	Experimental: high T (800–950°C)	Dislocation creep ± GSS[a] creep			$1.0 \times 10^{-2.97}$	183 ± 25	–	1.7 ± 0.2	0.51 ± 0.13	1.0 ± 0.2
Richter et al. (2018)	Experimental: high T (800–1,000°C)	Dislocation creep ± GSS[a] creep	General shear	Solid medium	3.1×10^{-4}	168–170	–	1.9 ± 0.6	~1.08	–
Hirth et al. (2001)	Compilation (experimental + natural)	Dislocation creep	N.A.	N.A.	6.3×10^{-12}	135 ± 15	–	4[b]	–	1
Lu & Jiang (2019)	Compilation	Dislocation creep	N.A.	N.A.	6.0×10^{-15}[c]	132 ± 5	35.3	4[b]	–	2.7
Tokle et al. (2019)	Compilation (experimental + natural)	Dislocation creep ± GSS[a] creep	N.A.	N.A.	8.0×10^{-12}	140 ± 15	–	4 ± 0.3	–	1
					5.4×10^{-12}	105 ± 15	–	2.7 ± 0.3	–	1.1

Note. N.A., not applicable.
[a]These studies reported evidence for variable amounts of grain size sensitive (GSS) creep. [b]Values for $n = 4$ are assumed from Luan and Paterson (1992) and Gleason and Tullis (1995). [c]Units are MPa^{-n-r} s^{-1}.

Fukuda and Shimizu (2017) use the silicic acid strain rate-stepping data from Luan and Paterson (1992) to calculate a value of $n = 3$ instead of $n = 4$. Tokle et al. (2019) assign different values to n ($n = 2.7$–3 and $n = 4$) based on the activation of rate-limiting easy slip systems at different temperatures and stresses. Numerous studies report values of $n < 3$, which are commonly interpreted to result from the activation of a grain size sensitive (GSS) deformation mechanism(s) (Kronenberg & Tullis, 1984; gel-origin experiments of Fukuda et al., 2018; Luan & Paterson, 1992; Richter et al., 2016, 2018). Further, the value of r shows similar variability as it is commonly resolved together with n from the same experimental data (Table 1).

2. Methods

2.1. Data Compilation

2.1.1. Selection of Experimental Data

Of the numerous experimental studies that have been carried out to constrain flow law parameters for crystal plastic behavior of quartz, we filter data by dominant deformation mechanism, water content, mechanical history, starting material, and composition to ensure consistency between experimental and natural deformation data sets. Filtering parameters are outlined in Appendix A. The full compiled data set is plotted in Figure 1 and tabulated in the Supplementary Material (Table S1).

2.1.2. Selection of Natural Data

We consider two field-based data sets that quantify deformation conditions precisely enough to assign specific strain rates to specific deformation conditions (Behr & Platt, 2011; Lusk & Platt, 2020). Strain rates from these studies are consistent with previous estimates measured or modeled in tectonically active midcrustal to lower-crustal regions (Hirth et al., 2001; Hughes et al., 2020; Lu & Jiang, 2019; Pfiffner & Ramsay, 1982; Sassier et al., 2009). For both these studies, electron backscatter diffraction crystallographic data were used to calculate dynamically recrystallized grain size and infer active slip system(s) and deformation mechanism(s). For consistency between studies, we take the reported grain size and recalculate differential stress using the piezometer of Cross et al. (2017). Temperature estimates from both regions are consistent with qualitative microstructural observations of recrystallization mechanism (Stipp et al., 2002) and active slip systems in quartz (Schmid & Casey, 1986; Takeshita, 1996; Toy et al., 2008). Natural data are included in Figure 1 and Table S1.

We do not use naturally constrained strain rate and deformation data from the RGD (Dunlap et al., 1997; Hirth et al., 2001), the Ailao Shan–Red River shear zone (ARSZ; Boutonnet et al., 2013; Sassier et al., 2009), nor the Cordillera Blanca shear zone (CBSZ; Hughes et al., 2019, 2020). In the RGD, Hirth et al. (2001) constrained strain rates within ~1.5 orders of magnitude (1×10^{-15} to 5×10^{-14} s^{-1}) and the differential stress to between 60 and 100 MPa (although dynamically recrystallized grain sizes reported by Dunlap et al. (1997) suggest that lower stresses were present). The uncertainties on their estimates are too large to be useful for the purposes of this paper. We do however compare our flow law parameters to the more broadly constrained deformation conditions in the RGD. In the ARSZ, Sassier et al. (2009) calculated strain rates from cross-cutting granitic dikes, and Boutonnet et al. (2013) calculated deformation conditions to investigate how strain rates calculated from flow laws for dislocation creep in quartz compared to those determined in the field. Similarly, Hughes et al. (2019, 2020) characterized deformation conditions and calculated independent, field-based, strain rates within the CBSZ. We do not include these data because in both the ARSZ and CBSZ rocks are granitic to granodioritic in composition and the authors did not demonstrate that quartz controls rock rheology.

Behr and Platt (2011) calculated deformation conditions of quartzofeldspathic gneisses deformed in the footwall of the Miocene, normal-sense Whipple Mountains metamorphic core complex (WMCC), eastern California. Here, the authors did demonstrate that quartz controls rock rheology, and independently quantified temperature, pressure, differential stress, and calculated a minimum shear strain rate of 1.6×10^{-11} s^{-1} for two samples in the lowest temperature, narrowest portion of the shear zone (PW34a, PW79a). This minimum strain rate was estimated using a cumulative shear zone width of 10 m (with upper and lower bounds of 20 and 5 m, respectively) and displacement rate of 5 mm $year^{-1}$.

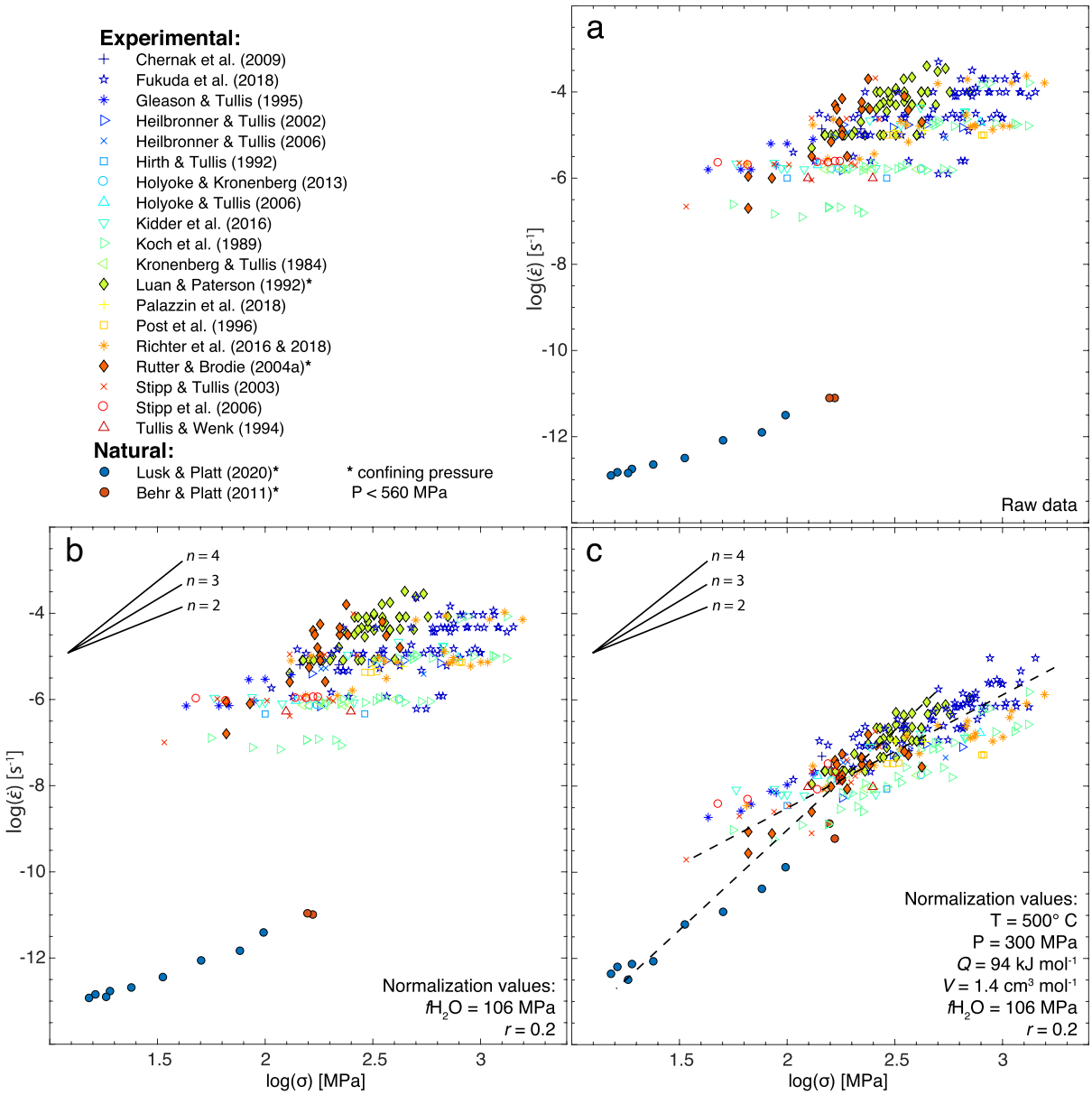

Figure 1. Plots of log(σ) and log($\dot{\varepsilon}$) with our complete experimental and natural data set illustrating the process of data normalization. (a) Data set normalized only for equivalent stress. (b) Data set normalized to a constant water fugacity, f_{H_2O} = 106 MPa, using r = 0.20. The value of r = 0.20 is based on the statistical analysis of the complete data set (Table 2). (c) Data set normalized to a constant f_{H_2O} as in (b) and to a constant temperature and pressure, T_{norm} = 500°C, P_{norm} = 300 MPa using H = 94 kJ mol^{-1} and V = 1.44 cm^3 mol^{-1} calculated from the statistical analysis of the complete data set. In (c), notice the striking difference in slope between data deformed at confining pressures <560 MPa (solid symbols with black outline), and the remainder of the data deformed at confining pressures >700 MPa (open symbols). The approximate best fit slopes are shown as dashed black lines, and the possible causes are discussed in the text.

Lusk and Platt (2020) estimated minimum equivalent strain rates and calculated deformation temperature and pressure as well as differential stress in the Late Ordovician to Silurian-aged Scandian shear zones (SSZs) of northwest Scotland. Strain rates are calculated based on a minimum displacement rate divided by shear zone width. A minimum displacement rate of 23 mm year^{-1} was calculated from total shortening over a time span bracketed by syn- and postkinematic intrusions. Shear zone width was reconstructed from detailed structural and microstructural observations (see Lusk & Platt, 2020 for further discussion). Minimum strain rates range from ~2×10^{-13} to ~4×10^{-12} s^{-1}. Two sets of mechanical data from this study, LS-72

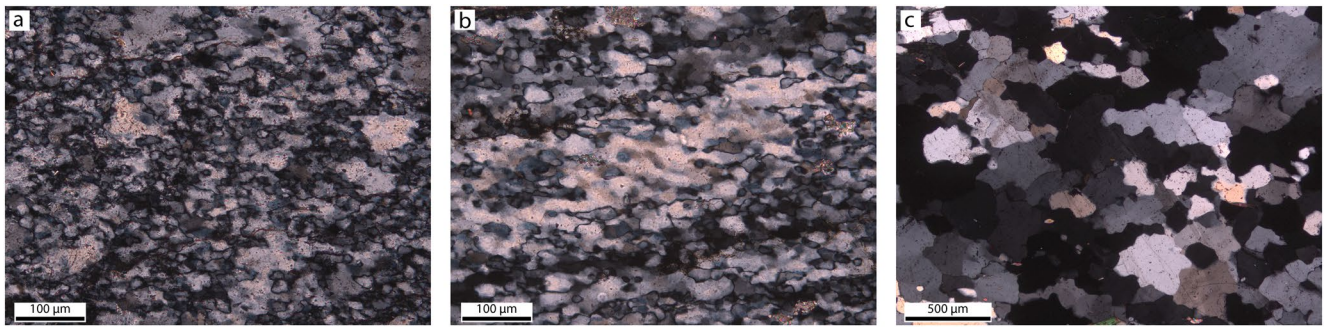

Figure 2. Sample photomicrographs representative of microstructures presented in Lusk and Platt (2020) illustrating the range of dislocation creep recrystallization mechanisms and similarity to microstructures produced in experimentally deformed samples (e.g., Gleason & Tullis, 1995, their Figures 4 and 7). (a) Recrystallization chiefly by bulge nucleation and minor subgrain rotation, roughly equivalent to Regimes 1 and 2 of Hirth and Tullis (1992). $T \approx 300$°C. (b) Microstructures found in the highest strain zone, recrystallized chiefly by subgrain rotation, comparable to Regime 2 of Hirth and Tullis (1992). $T \approx 350$°C. (c) Recrystallization by high-T grain boundary migration from structurally higher levels within the Scandian shear zone, roughly corresponding to Regime 3 of Hirth and Tullis (1992). $T \approx 400$–450°C. All images are in cross-polarized light and scales are indicated.

and LS-74, were disregarded from the analysis as they record anomalously low temperatures and stresses compared to adjacent samples.

Strain rate calculations from the SSZ and WMCC require assumptions about strain geometries and homogeneous distribution of shear and may also be susceptible to errors in calculated rates. The issues are discussed further in Lusk and Platt (2020). However, plotting these data in $\dot{\varepsilon}$–σ or $\dot{\varepsilon}$–T space, the uncertainty in naturally calculated strain rates is minor relative to the difference between experimental and natural conditions, making estimates sufficiently robust for the purpose of this study.

2.1.3. Comparing Natural and Experimental Deformation Mechanism(s)

Naturally and experimentally deformed quartz-rich mylonites must demonstrably deform by the same mechanism(s) if we are to confidently relate their mechanical behavior. Although we attempt to filter data to include only those in which dislocation creep produces the highest strain rate (i.e., it is the dominant deformation mechanism) we accept that in neither nature nor experiment do rocks deform by one single mechanism. Some experimental studies explicitly call on GSS creep (e.g., Fukuda et al., 2018; Richter et al., 2018; Rutter & Brodie, 2004b) as an active deformation mechanism, while others suggest that strain is accommodated almost exclusively by dislocation creep (e.g., Gleason & Tullis, 1995; Heilbronner & Tullis, 2002, 2006; Stipp & Tullis, 2003). Evidence for activity of GSS creep processes can be difficult to identify, especially in rocks where dislocation creep is dominant; an absence of direct evidence does not preclude GSS creep as a contributing deformation mechanism. We address this further in the discussion.

Both experimental and natural data used in this study record quartz microstructures consistent with strain accommodated primarily by dislocation creep. Quartz deformed by dislocation creep in natural mylonites recrystallizes by bulge nucleation, subgrain rotation, and high-temperature grain boundary migration, as outlined by Stipp et al. (2002). These three recrystallization mechanisms broadly correspond to the experimental Regimes 1–3, respectively, defined by Hirth and Tullis (1992). Likely because of the large differences between experimental and natural deformation conditions, Regime 3 of Hirth and Tullis (1992) is better related to the transitional subgrain rotation/high-temperature grain boundary migration zone of Stipp et al. (2002). In the SSZ and WMCC, rocks record evidence for multiple quartz recrystallization mechanisms including incipient recrystallization by bulge nucleation in the lowest temperature regions, transitioning to subgrain rotation, and finally to high-temperature grain boundary migration in the highest temperature regions (Behr & Platt, 2011; Lusk & Platt, 2020, Figure 2). Rocks from both locations record strong crystallographic preferred orientations (CPOs) indicative of dislocation creep along various slip systems (Schmid & Casey, 1986).

2.1.4. Corrections to Data

Experimental deformation conditions, including confining pressure, differential stress, temperature, and strain geometry, can vary significantly depending on experimental apparatus (e.g., solid or molten cell vs.

gas confining medium) and experimental goals. As such, the following corrections are applied to all data so that reported values of stress, strain rate, temperature, and confining pressure can be related to one another (Figure 1).

For calculations in this study, von Mises equivalent stresses and strain rates are used, following Tokle et al. (2019), using Equations 36 and 39 from Paterson and Olgaard (2000). For axial experiments, the equivalent stress equals the differential stress, and the equivalent strain rate equals the axial shortening rate. Experiments conducted in general shear are often reported as shear stress, τ, which we correct to an equivalent stress $\sigma_{\text{eff}} = \sqrt{3}\tau$ (Paterson & Olgaard, 2000). Likewise, shear strain rates, $\dot{\gamma}$, reported by experiments conducted in general shear are corrected to $\dot{\varepsilon}_{\text{eff}} = \frac{\dot{\gamma}}{\sqrt{3}}$.

Experiments carried out in a molten or solid cell apparatus may be prone to errors in differential stress measurement due to frictional forces on the load column, frictional or plastic forces on the sample, misidentification of the time at which a differential stress is first applied to a sample, or the strength of the confining material affecting the transfer of stresses to the sample (Holyoke & Kronenberg, 2010). A correction for comparing measured differential stresses from a solid cell apparatus to the more accurate gas apparatus was proposed by Holyoke and Kronenberg (2010). This correction remains a topic of active discussion (A. Kronenberg, C. Holyoke, G. Hirth, H. Stünitz, & R. Heilbronner, personal communication). Hirth and Beeler (2015) make the points that (1) the correction was determined on a single apparatus and results may not be applicable to other instruments, for example the instrument used by Stipp and Tullis (2003), and (2) there is agreement in sample strengths between the instrument used by Stipp and Tullis (2003) and a gas-medium apparatus. For these reasons, we have elected not to apply this correction to the data set, and any experimental data that applied the correction (e.g., Fukuda et al., 2018; Holyoke & Kronenberg, 2013) were recalculated to maintain consistency.

Water fugacity is calculated for each experimental and natural sample assuming a water activity of unity (validated for all experimental samples including at least 0.1–0.4 wt.% water) and pore fluid pressures equal to the confining pressure (assumed to be lithostatic for natural samples) using the Withers fugacity calculator, which solves the analytical expression from Sterner and Pitzer (1994) (www.esci.umn.edu/people/researchers/withe012/fugacity.htm).

2.2. Determination of Constitutive Parameters

Constitutive parameters for dislocation creep in quartz are often determined experimentally either in constant temperature experiments where the strain rate is stepped or at constant strain rate where the temperature is stepped. The strain rates of compiled rheological data can be normalized to either a constant temperature or constant stress to calculate n and H, respectively (Hirth et al., 2001; Tokle et al., 2019).

2.2.1. Stress Exponent

The stress exponent (n) is determined from the slope of the best fit line in $\log(\dot{\varepsilon})$–$\log(\sigma)$ space of a data set representing deformation at the same temperature. This is commonly achieved experimentally by conducting strain rate-stepping experiments at a constant temperature.

2.2.2. Activation Enthalpy

Activation enthalpy (H) is calculated in $\log(\dot{\varepsilon})$–$1/T$ space using data points that represent deformation at the same stress. The slope of a best fit line to the isostress data set is $-H/\text{R}$, where R is the universal gas constant. This is generally achieved experimentally by conducting temperature stepping experiments at a constant strain rate.

2.2.3. Water Fugacity Exponent

Water has a well-documented weakening effect on the strength of quartz and quartz aggregates (Griggs & Blacic, 1965; Kronenberg & Tullis, 1984). Following Paterson (1987, 1989), Kohlstedt et al. (1995) suggested that the effect of water on the ductile strength of quartz may be expressed by the addition of a water fugacity

($f_{H_2O}^r$) term to the constitutive equation for dislocation creep (Equation 1). Water fugacity is strongly sensitive to changes in pressure while only moderately sensitive to changes in temperature.

To determine the magnitude of the fugacity exponent experimentally and isolate the effect of f_{H_2O}, studies are conducted either at constant strain rate and temperature, while stepping the confining pressure and measuring the resulting steady-state flow stress, or with variable fluid compositions (e.g., Chernak et al., 2009; Post et al., 1996). In $\log(\sigma)$–$\log(f_{H_2O})$ space at constant strain rate and temperature, the slope of a best fit line, M, is equal to $-r/n$.

2.2.4. Activation Volume

There is strong evidence in support of a pressure-sensitive activation enthalpy in silicate minerals such as olivine and feldspar (e.g., Karato & Jung, 2003; Rybacki et al., 2006) and recent work has attempted to quantify this pressure sensitivity in quartz (Lu & Jiang, 2019). Lu and Jiang (2019) determined the activation volume, V, by iterative linear regression using three data points from the pressure-stepping experiments of Kronenberg and Tullis (1984) and obtained a value of 35.3 cm^3 mol^{-1}. However, as discussed in Chernak et al. (2009), the agreement between water fugacity sensitivity in their experiments conducted at constant pressure with variable fluid composition, compared to the pressure-stepping experiments from Kronenberg and Tullis (1984), suggests that the activation volume in quartz is small.

2.3. Calculations

2.3.1. Bayesian Statistical Analysis

We have analyzed the data set using the Markov Chain Monte Carlo (MCMC) method (Metropolis et al., 1953). This estimates best fit values for the parameters in the flow law by exploring parameter space along a path known as a Markov chain. This is defined as a memoryless probability model of a stochastic process, which means that each step depends only on the previous state and not on the history of the model. At each point in the chain, MCMC determines how well the parameter values at that point fit the data set. As it explores parameter space, it builds a probability density function (PDF) for the goodness of fit, which it evaluates by minimizing a loss function which is the negative log(probability); for example, the squared loss $||\text{prediction} - \text{data}||^2$. An advantage of MCMC methods versus other search algorithms is that it gives bounds on the parameters.

An exhaustive search through high-dimensional parameter space using the Markov Chain method would be very inefficient. There are various strategies for guiding the trajectories of the Markov chains into significant volumes of parameter space where the fit is good. We have used the Hamiltonian strategy, which uses analogies between the exploration strategy and the formalisms of classical mechanics and greatly reduces the computational time involved (Neal, 1995, 2011). We analyzed the data using an open-source package called pymc3, written in Python, which implements the Hamiltonian strategy for MCMC with an initialization routine called NUTS (No U-Turn Sampler; Salvatier et al., 2016). The program typically uses multiple Markov chains to map out the PDF, which allows us to compute some convergence statistics and makes it more likely that we have an unbiased sample. If the PDF has a Gaussian form, the mean value for each parameter is easily determined, together with standard deviation. If the PDF is strongly skewed, the most useful value is less obvious. For a log-normal distribution, the modal value indicates the highest likelihood, but the median value (which is the peak of the log distribution) gives the best fit with the other parameters. Covariance plots can provide insight into the trade-offs among the different parameters (Foreman-Mackey, 2016).

Initial MCMC analysis on the entire data set gave surprising results, including a value of r that was effectively zero (Figures 3a, S1a, and S2; Table 2). Further analysis showed that this was a result of the large number of data points representing experiments performed at high pressure and temperature, which have similar water fugacities (e.g., Fukuda et al., 2018; Koch et al., 1989), and dominated the sample population. If all the fugacity values are similar, the most probable solution is that it has no effect; hence $r = 0$. To circumvent this issue, we picked a reduced sample set representative of the full data set and carried out an MCMC analysis to solve for parameters n, r, Q, V, and A. The reduced sample set includes all of the natural data, plus experimental data picked based on the following routine. The experimental data were first divided

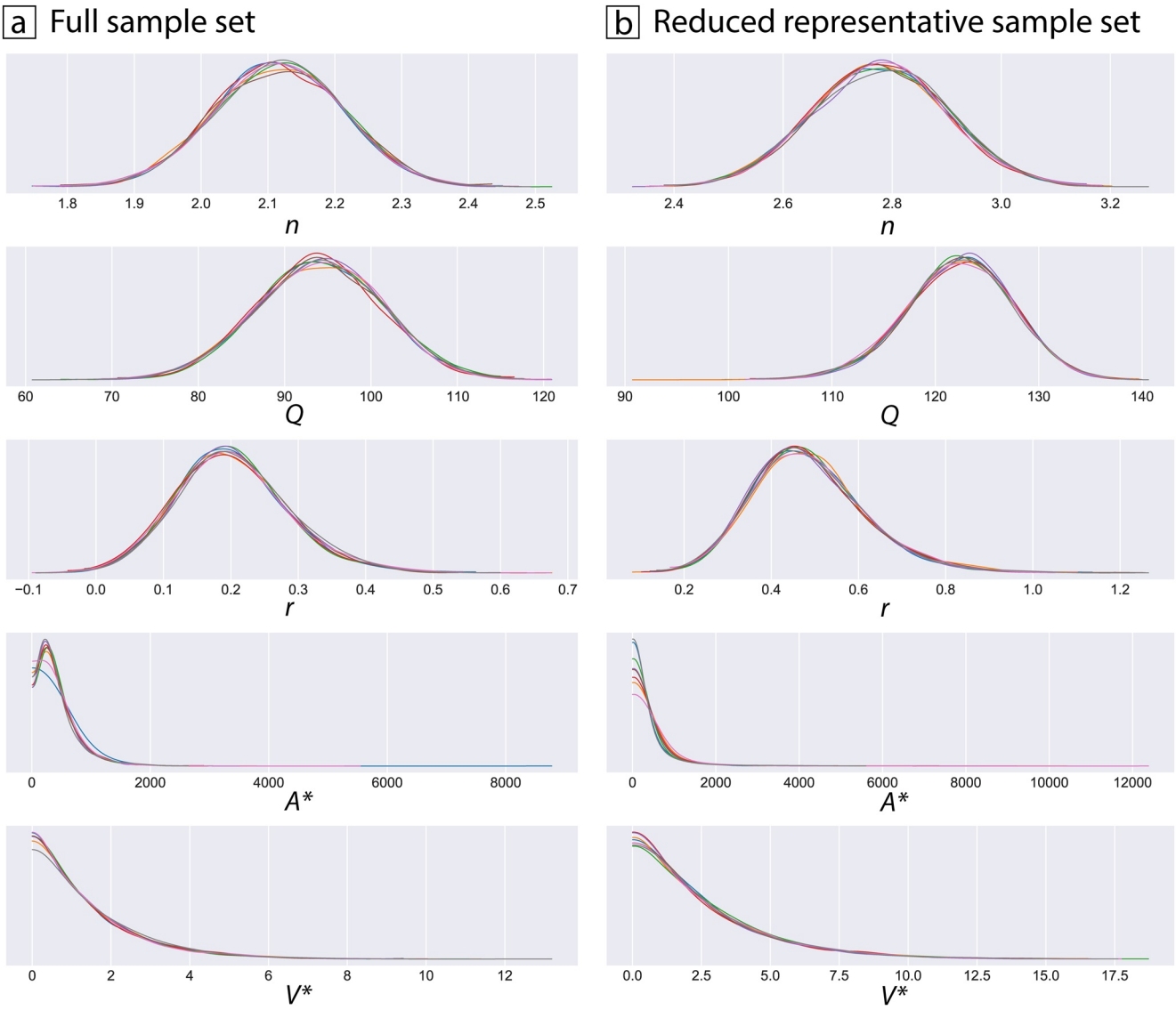

Figure 3. Probability distribution functions for the full sample set (a) and the reduced representative sample set (b) for five-variable MCMC (Markov Chain Monte Carlo) analyses. For the statistical analysis, values of $A^* = A \times 10^9$ and $V^* = V \times 10^9$ for the full sample set (a) and $A^* = A \times 10^{10}$ and $V^* = V \times 10^6$ for the reduced representative sample set (b) were used. In both cases, A^* is given as the natural log and therefore differs from values cited in the text.

Table 2
Flow Law Parameters Determined by Markov Chain Monte Carlo Analysis on Different Data Sample Sets

Data Set	Prefactor log(A) (MPa^{-n-r} s^{-1})	Activation energy Q (kJ mol^{-1})	Stress exponent n	Activation volume V (cm^3 mol^{-1})	Water fugacity exponent r
Full	−6.36 + 0.25/−0.69	94 ± 7	2.1 ± 0.1	1.44 ± 1.43	0.20 ± 0.08
Representative reduced	−7.74 + 0.52/−0.57	122 ± 5	2.8 ± 0.1	2.59 ± 2.45	0.49 ± 0.13
Low pressure	−9.30 ± 0.66	118 ± 5	3.5 ± 0.2	2.59 ± 2.45[a]	0.49 ± 0.13[a]
High pressure	−7.90 ± 0.34	77 ± 8	2.0 ± 0.1	2.59 ± 2.45[a]	0.49 ± 0.13[a]

Note. These are discussed further in the text.
[a]From "representative reduced."

into three pressure bins (300, 700–1,270, and 1,300–1,600 MPa). These bins were then subdivided into 100° temperature bins. Within these temperature bins, 6–8 data points were picked covering the full range of stress present. This reduced the total data set from 271 to 83 without introducing bias in terms of pressure, temperature, or stress. Data used in this reduced sample set are plotted with the full data set in Figure S3.

We start with the assumption that the same constitutive relationship can describe both the natural data and all of the experimental data. A MCMC analysis of the reduced representative sample set produced the following parameters $n = 2.8 \pm 0.1$; $r = 0.49 \pm 0.13$; $Q = 122 \pm 5$ kJ mol^{-1}; $V = 2.59 \pm 2.45$ cm^3 mol^{-1}; and $\log(A) = -7.74 + 0.52/-0.57$ MPa^{-n-r} s^{-1} (Figures 3b, S1b, and S3; Table 2). Values of r, Q, and V were then used to normalize the full data set to a constant water fugacity, temperature, and pressure, and normalized data were plotted in $\log(\dot{\varepsilon})$–$\log(\sigma)$ space to evaluate the fit of data to a single stress exponent (Figure 1c). The complete data set clearly shows two distinct slopes, or *effective* stress exponents, indicating that a single constitutive relationship does not sufficiently describe the complete data set. Tokle et al. (2019) recognized a variation in stress exponent in compiled quartz experimental deformation data and attributed it to the activation of different rate-limiting slip systems in response to temperature and stress. By contrast, we observe that all samples deformed at confining pressures <700 MPa consistently plot along a slope of $n \approx 4$, while samples deformed at higher confining pressures (>700 MPa) plot along a more gentle slope, closer to $n \approx 2$. While there may be an influence of slip system on n, this observation suggests that a more fundamental difference may be the confining pressure at which experiments were conducted.

Ductile behavior of quartz aggregates thought to be deforming primarily by dislocation creep have been shown to be sensitive to pressure (Kronenberg & Tullis, 1984; Lu & Jiang, 2019). This sensitivity is attributed to the pressure dependence of the water fugacity (Kohlstedt et al., 1995; Paterson, 1987, 1989), an activation volume in the activation enthalpy term (Lu & Jiang, 2019), and/or activation of additional deformation mechanisms that are sensitive to pressure (e.g., pressure solution; Kronenberg & Tullis, 1984; Paterson & Luan, 1990; Richter et al., 2018). Normalization to a constant water fugacity, temperature, and pressure in Figures 1b and 1c, respectively, indicates that water fugacity and activation volume alone cannot account for the observed effect of confining pressure.

2.3.2. Pressure Binning

Motivated by this observation, we grouped the natural and full experimental data sets by the confining pressure during deformation, to further investigate the potential effects of pressure on the effective stress exponent. Compiled data are grouped into "low-pressure" (confining pressure <560 MPa) and "high-pressure" (confining pressure 700–1,600 MPa) sample sets, as discussed below.

2.3.2.1. Selection of Pressure Ranges

Naturally deformed rocks from the WMCC and SSZ span a range of confining pressures from 240 to 560 MPa, significantly lower than is attained in many experiments using the Griggs apparatus, but much closer to conditions within a Paterson apparatus (300 MPa). We select all 11 field samples to combine with 40 experiments conducted at a confining pressure of 300 MPa (from Luan & Paterson, 1992; Rutter & Brodie, 2004b). Similarly, we group data derived from Griggs apparatus experiments deformed between 700 and 1,600 MPa. However, determination of both r and V requires using a data set that spans the full range of confining pressures. We therefore used the values of $r = 0.49 \pm 0.13$ and $V = 2.59 \pm 2.45$ cm^3 mol^{-1} determined from the MCMC analysis of the reduced representative sample set (Figures 3b, S1b, and S3). We then reanalyzed the "high-pressure" and "low-pressure" data sets separately by MCMC for which we recalculate the parameters n, Q, and A to arrive at a composite flow law for dislocation-dominated creep in quartz.

In addition to reducing the effects of pressure, including experimental data only from Paterson-type deformation experiments in the "low-pressure" sample set has the advantage of more precise measurements of the differential stress applied to samples. Friction corrections, necessary because of the solid or molten confining medium used in a Griggs apparatus, contain large uncertainties resulting in measured stress errors that are difficult to quantify (Gleason & Tullis, 1993). Friction corrections are not as important for strain rate-stepping experiments where stresses are measured relative to a common reference point (e.g., hit point) but are critically important when comparing data from different experiments or labs. The correction proposed by Holyoke and Kronenberg (2010) discussed above does not account for variable practices between labs, for example in determining the "hit point," or in sample preparation. We note

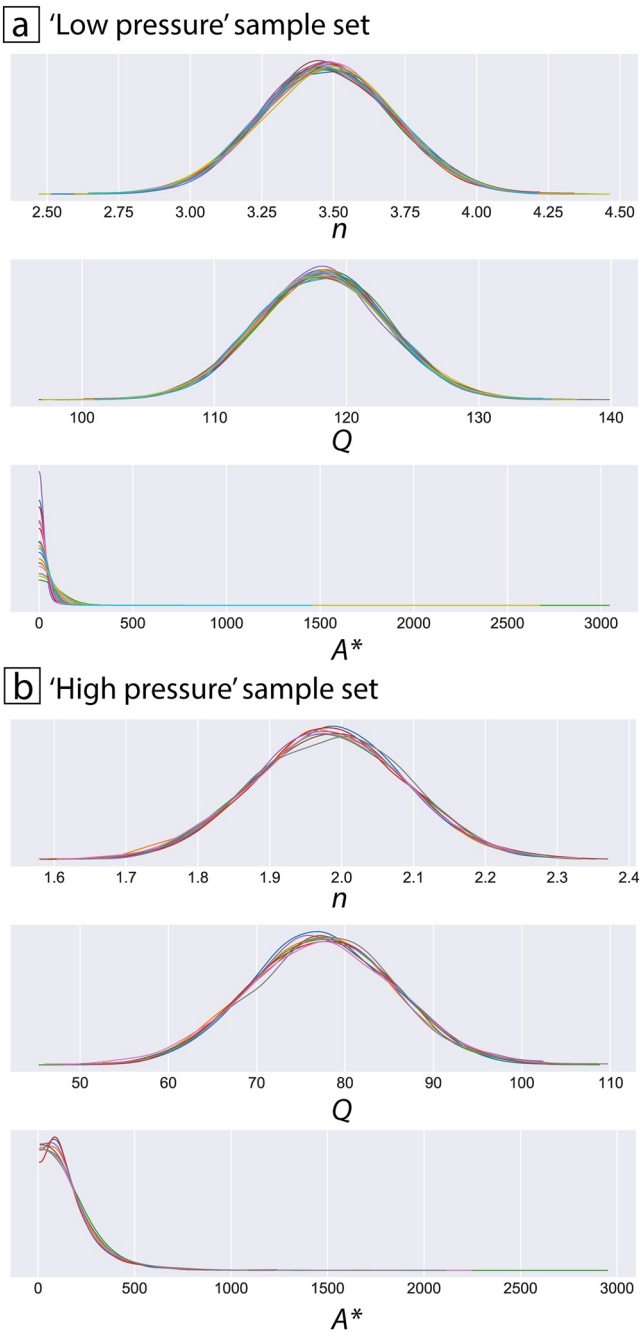

Figure 4. Probability distribution functions for the "low-pressure" (a) and "high-pressure" (b) data sets for three-variable MCMC (Markov Chain Monte Carlo) analyses. For the statistical analysis, $A^* = A \times 10^{10}$ for both (a) and (b). Note that here, A^* is given as the natural log.

however that stress estimates of naturally deformed samples are derived from an empirical piezometric relationship determined by experiments performed on a Griggs apparatus, although other work indicates consistency in measured stresses between the apparatus used by Stipp and Tullis (2003) and a gas-medium apparatus (Hirth & Beeler, 2015 supplement and references therein).

3. Results

3.1. Reduced Pressure Range Investigations

We performed MCMC analyses of the "low-pressure" and "high-pressure" data sets, solving for n, Q, and A, assuming values for r and V from the MCMC analysis of the representative reduced sample set. The "low-pressure" data set yields (Figures 4a and 5a; Table 2)

$$\dot{\varepsilon} = 10^{-9.3\pm0.7}\sigma^{3.5\pm0.2} f_{H_2O}^{0.49\pm0.13} e^{-\frac{118{,}000\pm5{,}000+(2.59\pm2.45P)}{RT}} \quad (3)$$

The "high-pressure" data set yields a significantly different set of parameters (Figures 4b and 5b; Table 2):

$$\dot{\varepsilon} = 10^{-7.9\pm0.3}\sigma^{2.0\pm0.1} f_{H_2O}^{0.49\pm0.13} e^{-\frac{77{,}000\pm8{,}000+(2.59\pm2.45P)}{RT}} \quad (4)$$

where σ, f_{H_2O}, and P are in MPa and T is in degrees K. Uncertainties in parameter values are reported as 1 s.d. from the mean for σ, n, r, Q, and V, whereas A is reported as 1 s.d. from the median because of the log-normal distribution (Figure 5).

To check the fit and internal consistency of these calculated parameters on the individual data sets, we normalized data to a constant water fugacity and temperature using values of r, Q, and V calculated by MCMC analysis to check the stress exponent, n, by plotting data in $\log(\dot{\varepsilon})$–$\log(\sigma)$ space (Figures 6a and 7a). Similarly, we used values of r and n calculated by MCMC analysis to normalize data to a constant water fugacity and stress (T_{std} = 900°C; P_{std} = 1,500 MPa; f_{H_2Ostd} = 5,030 MPa; σ_{std} = 500 MPa, and T_{std} = 500°C; P_{std} = 300 MPa; f_{H_2Ostd} = 106 MPa; σ_{std} = 200 MPa for high- and low-pressure data sets, respectively) then plotted normalized data in $\log(\dot{\varepsilon})$–$1/T$ space to check our calculated values of activation enthalpy, H (Figures 6b and 7b). For each of these plots, we used an orthogonal regression to calculate the value of n and H predicted by data sets normalized to parameters from the MCMC analyses. The "low-pressure" data set yields n_{ortho} = 3.8 ± 0.2 and H_{ortho} = 119 ± 5 kJ mol^{-1}, and the "high-pressure" data set gives n_{ortho} = 2.6 + 0.3/−0.2 and H_{ortho} = 155 + 37/−27 kJ mol^{-1} (Figures 6 and 7). The reader should note that values calculated in $\log(\dot{\varepsilon})$–$1/T$ space give an activation *enthalpy*, H; however, the value of V is small enough that the effect of VP is negligible.

4. Discussion

4.1. Consistency of Calculated Parameters and Comparison to Previously Published Values

4.1.1. Fugacity Exponent and Activation Volume

Our calculated values of r and V, used in both the "low-pressure" and "high-pressure" data set MCMC analyses, are lower than most previous estimates. Our calculated value of r = 0.49 ± 0.13 is smaller than values

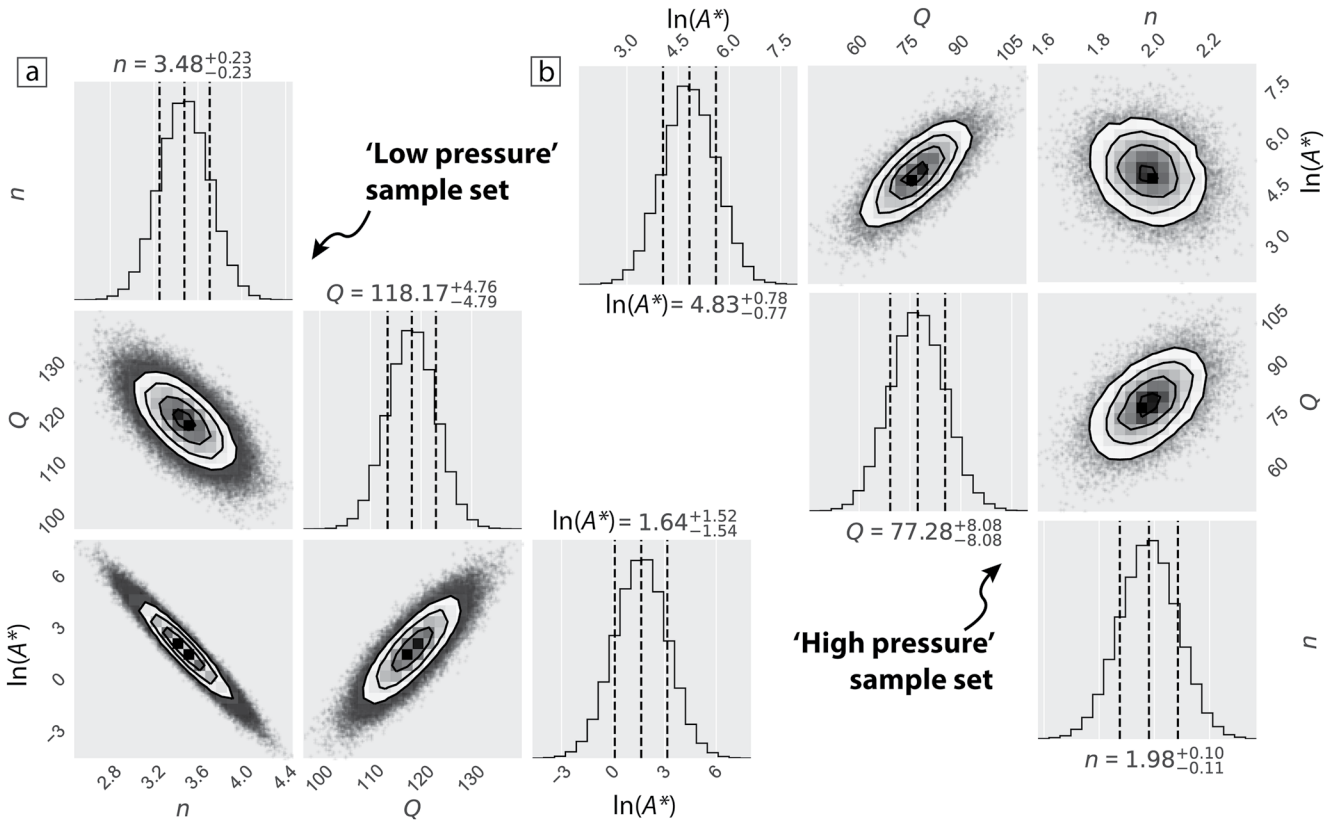

Figure 5. Probability distribution functions and covariance density plots from MCMC (Markov Chain Monte Carlo) analyses of "low-pressure" (a) and "high-pressure" (b) sample sets. Dashed lines are mean values and associated uncertainties, expressed as 1 s.d. from the mean, for n and Q. $A^* = A \times 10^{10}$. The values of ln(A^*) are taken as the median due to the log-normal distribution. Point clouds are contoured at higher densities to illustrate distribution details. Note that because of the statistical analysis, A^* is given as natural log on the corner plots, whereas in the text, we use $\log_{10}$. Plots were made using scripts from Foreman-Mackey (2016).

from many previous studies that commonly calculate or estimate $r \approx 1$ (Table 1, Kohlstedt et al., 1995) or higher (e.g., $r = 2.5$; Holyoke & Kronenberg, 2013). For rocks deformed in the RGD, Hirth et al. (2001) found that $r = 1$ fit natural rock data better than $r = 2$. Likewise, Tokle et al. (2019) calculated values of $r = 1$, 1.1, and 1.2 based on compiled experimental data, and Kohlstedt et al. (1995) suggest $0.8 \leq r \leq 1.2$ using experimental data from Kronenberg and Tullis (1984) and a value of n from Gleason and Tullis (1995) and Luan and Paterson (1992).

When calculated by pressure-stepping experiments, the value of r requires an independent determination of n (see Section 2.2.3). Explicitly, the best fit line in log(σ)–log(f_{H_2O}) space, $M = -r/n$. Although not a rheological parameter, M can be useful in comparing the water fugacity exponent independent of n; typical values from pressure-stepping experiments indicate $M \approx -0.50$ (Table S2). New experimental results by Negré et al., not yet published at the time of this study, calculated $M = -0.46$, consistent with this average value (personal communication with Holger Stünitz). Chernak et al. (2009) conducted constant pressure experiments at variable fluid activity and chemistry, arriving at a best fit value of $M = -0.23$ (for all data points), while the overall variation in their sample strengths was consistent with $-0.13 \leq M \leq -0.25$. The MCMC approach does not calculate r as a function of n, but from the calculated values of r and n, we arrive at $M_{LP} = -0.14$ and $M_{HP} = -0.25$. Regardless of binning, values of M "determined" by the MCMC approach remain smaller than those determined from pressure-stepping experiments but overlap with values from Chernak et al. (2009).

Although $r = 0.49$ is smaller than experimental determinations, we suggest this value may be consistent with what is predicted by theory based on hydrolytic weakening due to hydrolysis of Si–O bonds. There are several proposed mechanisms that may account for observed hydrolytic weakening in quartz (e.g.,

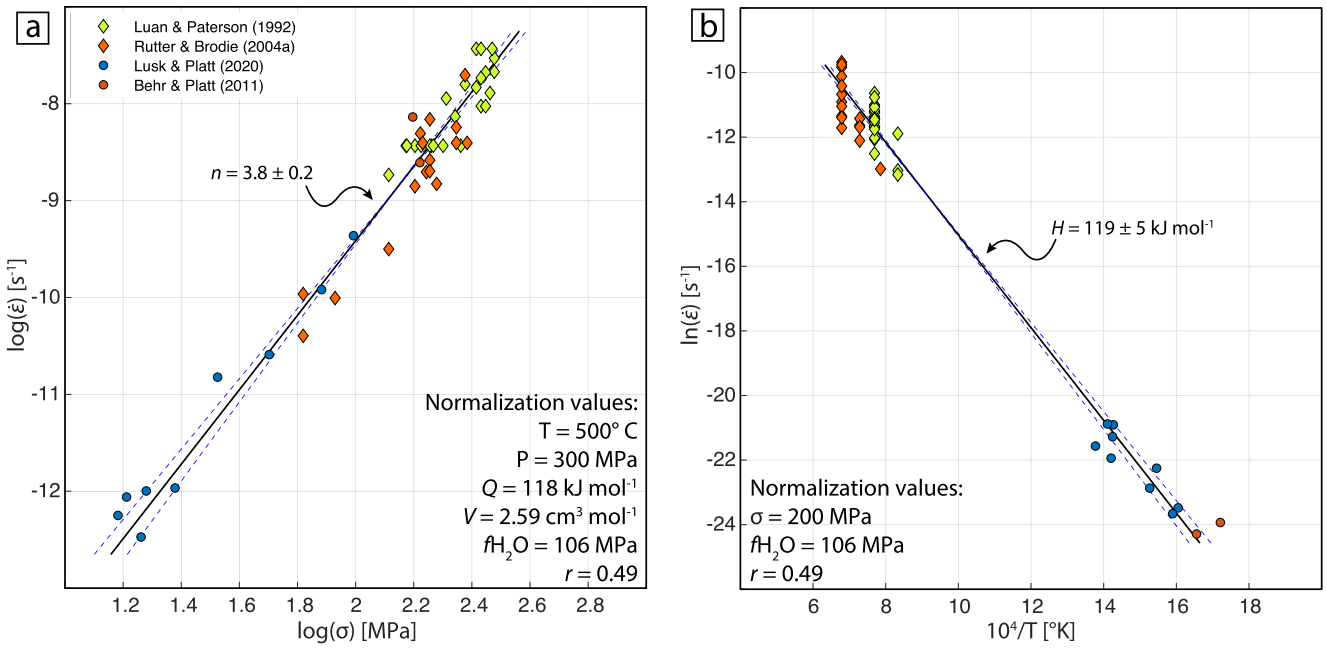

Figure 6. Check of internal consistency by calculating the stress exponent (a) and activation *enthalpy* (b) for the "low-pressure" data set, normalizing data using parameter values from the "low-pressure" MCMC (Markov Chain Monte Carlo) analysis (Table 2). Orthogonal regression model lines shown with confidence bounds (dashed). Calculated values with 95% confidence interval as follows: (a) $n = 3.8 \pm 0.2$ and (b) $H = 119 \pm 5$ kJ mol^{-1}. Note the significantly larger range to lower values of stresses (a) and temperatures (b) introduced by the addition of natural data. Normalization values and data sources are noted on the figure panels.

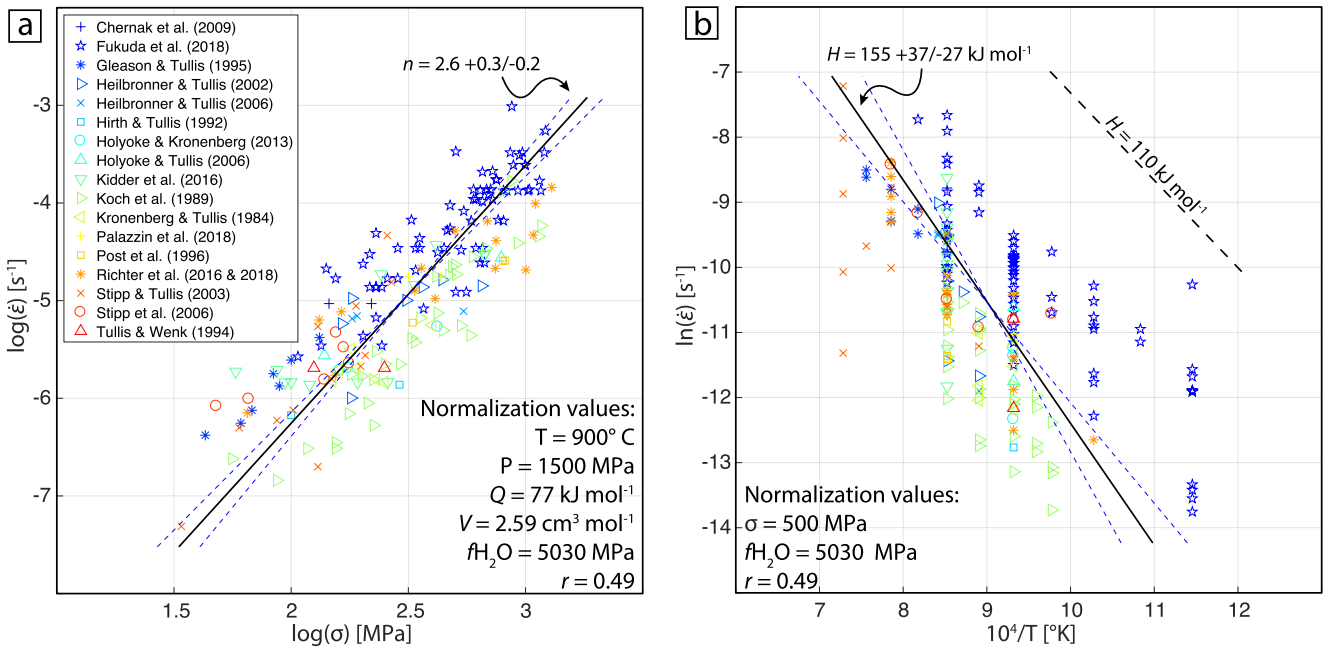

Figure 7. Check of internal consistency by calculating the stress exponent (a) and activation *enthalpy* (b) for the "high-pressure" data set normalizing data using parameter values from the "high-pressure" MCMC (Markov Chain Monte Carlo) analysis (Table 2). Orthogonal regression model lines shown with confidence bounds (dashed). Calculated values with 95% confidence interval error as follows: (a) $n = 2.6 + 0.3/-0.2$ and (b) $H = 155 + 37/-27$ kJ mol^{-1}. Normalization values and data sources are noted on the figure panels.

crystalline hydrogen ion defects, hydroxyl defects, or grain boundary effects—see Kronenberg, 1994). If the dominant mechanism is hydrolysis of siloxane groups (Si–O–Si) to produce silanol groups (Si–OH), a substitution nucleophilic bimolecular (S_N2) reaction can be written as a single water molecule (H_2O) reacting with a siloxane group (representing two SiO_4 tetrahedra):

$$\text{Si–O–Si} + H_2O \rightarrow \text{Si–OH} : \text{HO–Si} \quad (5)$$

The law of mass action therefore dictates that the effect of hydrolysis of siloxane groups on quartz dislocation creep depends on the square root of the water activity, and hence also on the square root of the water fugacity (the distinction between the activity and fugacity being the choice of standard state).

Our value of $V = 2.59 \pm 2.45$ cm^3 mol^{-1} is significantly lower than 35.3 cm^3 mol^{-1} for quartz estimated by Lu and Jiang (2019) and is also lower than values of other silicate minerals (e.g., $V_{olivine} = 15 \pm 5$ (dry), 14 ± 2 (dry), 24 ± 3 (wet) cm^3 mol^{-1}, $V_{feldspar} \approx 24$ (dry), 38 (wet) cm^3 mol^{-1}; Dixon & Durham, 2018; Karato & Jung, 2003; Rybacki et al., 2006). The low value calculated here is consistent with observations from Chernak et al. (2009) that the activation volume should be small, based on agreement between the effect of water fugacity from experiments conducted at constant temperature and pressure, with variable fluid composition (e.g., Chernak et al., 2009) and those conducted with pure water at constant temperature but variable pressure (e.g., Kronenberg & Tullis, 1984). The reader should note that the error is only large relative to the small value of V.

An assumption we make in carrying constant values of r and V through to the low- and high-pressure analyses is that both of these values hold constant over the investigated parameter space. Because each parameter requires a significant range of pressures to calculate, the binning of sample sets into smaller pressure ranges is unsuitable for independently estimating r and V.

4.1.2. "Low-Pressure" Data Set

The activation energy calculated in this analysis, $Q = 118 \pm 5$ kJ mol^{-1}, is close to within error of many previous estimates. The calculated stress exponent, $n = 3.5 \pm 0.2$ is notably lower than the commonly accepted value of $n = 4$, although it remains within error of some experimental determinations (Table 1). The calculated value for n is consistent with a model for steady-state dislocation creep proposed by Weertman (1968) in which strain is accommodated by dislocation glide yet rate controlled by climb. In this model, if the density of dislocation sources is itself dependent on stress, a theoretical value of $3 \leq n \leq 3.5$ is predicted.

Parameter values calculated by MCMC analysis are both within error of values calculated by orthogonal regression of normalized data; $Q_{MCMC} = 118 \pm 5$ kJ mol^{-1} versus $H_{ortho} = 119 \pm 5$ kJ mol^{-1}, and $n_{MCMC} = 3.5 \pm 0.2$ versus $n_{ortho} = 3.8 \pm 0.2$ (Figure 6). One possible reason for the discordance between results from MCMC and orthogonal linear regression is that assumptions inherent in linear regression are not fully met (e.g., homoscedasticity, independence of errors, or valid approximation as a Gaussian distribution), whereas the MCMC method requires none of these assumptions.

The greatest extrapolation in experimental versus natural conditions besides the strain rate is temperature. Therefore, small discrepancies in H calculated experimentally may cause sizable errors when extrapolating to geological conditions. By significantly increasing the range of temperatures used to determine H (i.e., both Q and V), we believe calculations integrating the relatively low temperature and slow strain rate natural data produce a more robust constitutive relationship for quartz dislocation-dominated creep at geological conditions, compared to those derived purely from experimental data sets. However, we again remind the reader that the natural data used in this study are not completely independent due to calculation of differential stress by experimentally calibrated paleopiezometry.

4.1.3. "High-Pressure" Data Set

The activation energy calculated for the high-pressure experimental compilation, $Q = 77 \pm 8$ kJ mol^{-1}, is significantly lower than previous estimates. The calculated stress exponent, $n = 2.0 \pm 0.1$, while lower than the commonly cited value of $n \approx 4$, and outside the range of theoretical values (3–5), is in fact consistent with many other experimental studies that estimate values in the range of $1.7 < n < 2.9$ (Table 1). Unlike the "low-pressure" data set, the "high-pressure" parameter values calculated by MCMC analysis are less consistent with parameter values calculated by orthogonal regression of normalized "high-pressure" data;

Table 3
Slopes of the First Three Principal Components Expressed in Terms of the Five Constitutive Variables

	ln ε	ln σ	ln $f(H_2O)$	P	T
1	0.5342	−0.4931	0.4720	−0.4898	0.0943
2	0.1407	−0.0558	0.6065	0.7594	−0.1802
3	−0.3519	0.5760	0.6142	−0.3236	0.2499

$Q_{MCMC} = 77 \pm 8$ kJ mol^{-1} versus $H_{ortho} = 155 + 37/-27$ kJ mol^{-1}, and $n_{MC\text{-}MC} = 2.0 \pm 0.1$ versus $n_{ortho} = 2.6 + 0.3/-0.2$ (Figure 7). The significantly higher value and large uncertainty on the value of H reflects the heterogeneous distribution of "high-pressure" data. A paucity of data at the low- and high-temperature extremes results in the fit of the orthogonal regression being strongly affected by data clustered at moderate temperatures and leads to a slope steeper than the overall distribution, and hence a higher value of H. A dashed line with a slope of 110 kJ mol^{-1}, which is more consistent with the "low-pressure" analysis and previous determinations, is plotted alongside the "high-pressure" data and qualitatively appears to show a better fit compared to the orthogonal regression line (Figure 7b). As with the "low-pressure" data set, the discordance between MCMC and linear regression calculations may be due to linear regression assumptions not being satisfied. Despite the lack of internal consistency between methods, they are consistent in predicting a lower value of n for the "high-pressure" data set compared to the "low-pressure" data set, which we discuss further below.

4.2. Evaluating Flow Laws by Principal Component Analysis

To test how well the results of the MCMC analysis fit the data, we have also performed principal component analysis (PCA) on the data set. Because of the problems we encountered using MCMC analysis on the full data set, we applied PCA to the same reduced data set that we used for MCMC analysis. The reduced data set encompasses the full variance of all the observational variables but thins out the number of experimental data points, in particular the high-pressure experimental data.

PCA rotates the data in N-dimensional space, where N is the number of observational variables (5 in this case: strain rate, stress, temperature, confining pressure, and water fugacity), in order to determine the principal axes, or eigenvectors, of the distribution. This enables the data to be viewed in a reduced number of dimensions: in our case, 95% of the variance can be represented in two dimensions and 99.7% in three dimensions. To facilitate the analysis, we took the natural logarithm of the flow law equation:

$$\ln \dot{\varepsilon} = n \ln \sigma + r \ln f_{H_2O} - \left(Q + PV\right) / RT \tag{6}$$

and used $\ln \dot{\varepsilon}$, $\ln \sigma$, $\ln f_{H_2O}$, P, and $1/T$ as the variables. To perform the analysis, each variable is centered about its mean, and the variables have to be scaled so that they have similar ranges. We carried out this scaling manually, multiplying $\ln \dot{\varepsilon}$ by 0.5, P (in MPa) by 0.007, and $1/T$ by 10^4. The analysis was carried out using the PCA module in Matlab®. The slopes of the first three principal components, expressed in terms of these variables, are listed in Table 3. The percentage of the total variance expressed by each of the five principal components are 1, 67.48%; 2, 27.32%; 3, 4.84%; 4, 0.27%; 5, 0.08%.

The observational data are shown on two-dimensional (2D) and three-dimensional (3D) plots (Figure 8) by the red filled circles. The plotting routine rescales the data, so that quantitative information cannot be obtained from them, but they allow the different data sets to be distinguished, and how they are distributed relative to the observational variables. To test how well the flow law parameters determined by the MCMC analysis fit the observations, we have recalculated the strain rates using the values for A, n, r, Q, and V that we determined for the "low-pressure" and "high-pressure" data sets. These are plotted as open blue circles in the figures. The only difference between the observed and calculated data sets is the strain rate, so if the calculated strain rates do not fit the observations, they are displaced parallel to the strain rate axis.

Figure 8a shows that the "low-pressure" parameter values fit both the field and the low-pressure experimental data clusters well, whereas the medium and high-pressure clusters show significant offsets. This validates the results of the MCMC analysis for the "low-pressure" data. Conversely, Figure 8b shows that the "high-pressure" parameter values fit the highest pressure data cluster reasonably well, and the "low-pressure" and field clusters poorly. The moderate pressure cluster shows variable offsets tending to decrease with increasing pressure. These variations reflect how the different values of n control the strain rate of the "low-pressure" versus the "high-pressure" clusters and suggest that the change in n occurs gradationally

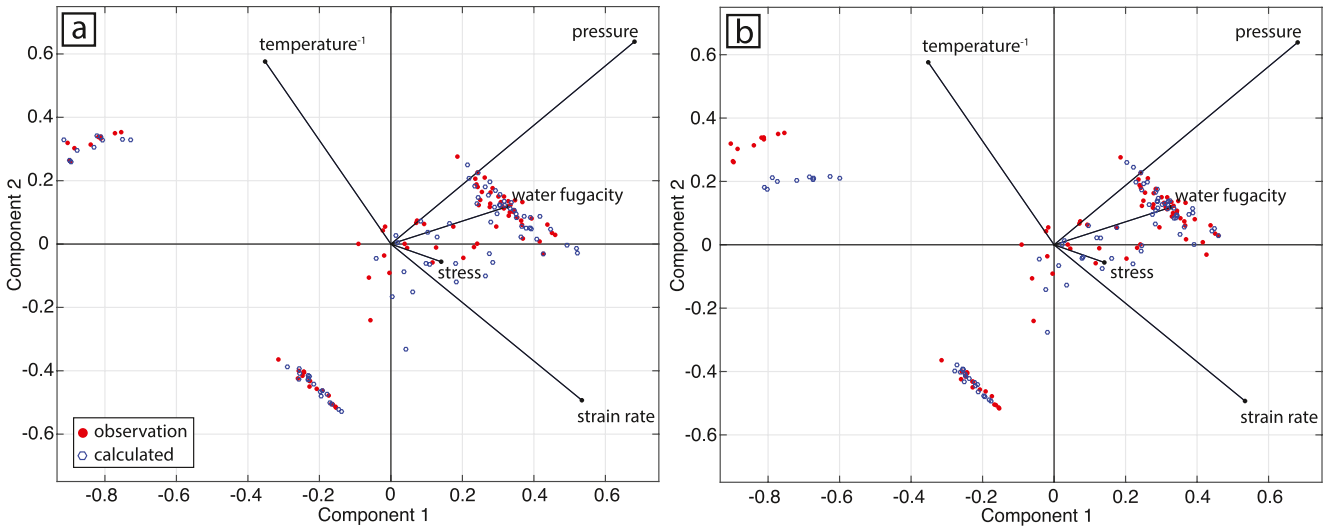

Figure 8. The reduced data set plotted relative to the first two principal component axes (see text for the method and the coefficients of the axes). Red filled circles are the observations; blue open circles have strain rate values calculated using the flow law parameters determined by MCMC (Markov Chain Monte Carlo) analysis. (a) Comparison using the "low-pressure" parameters. Field observations plot in the top left, low *P* experimental data in the bottom left, high *P* data in the top right, and intermediate pressure data across the center of the plot. Note that the data set as a whole is centered about the means of the variables. The calculated values fit the field and low-pressure experimental data well, and the intermediate and high-pressure data poorly. (b) Comparison with results calculated using the "high-pressure" flow law parameters. The calculated values fit the high-pressure experimental data well and the field and low-pressure data poorly. The fit for the intermediate pressure data improves progressively with increasing pressure.

over the pressure range of the medium pressure data set. This validates the results of the MCMC analysis for the "high-pressure" data sets.

Figure 9 plots 3D views with calculated results using the "high-pressure" parameter values (fully 3D plots of both the "high-pressure" and the "low-pressure" data are available as supplementary material Figures S6 and S7). Figure 9a looks straight down the strain rate axis, which demonstrates that the difference between the observed and calculated results lies along this axis. Figure 9b is a view normal to the plane containing the temperature and strain rate axes. These show that the offsets between the observed and calculated data

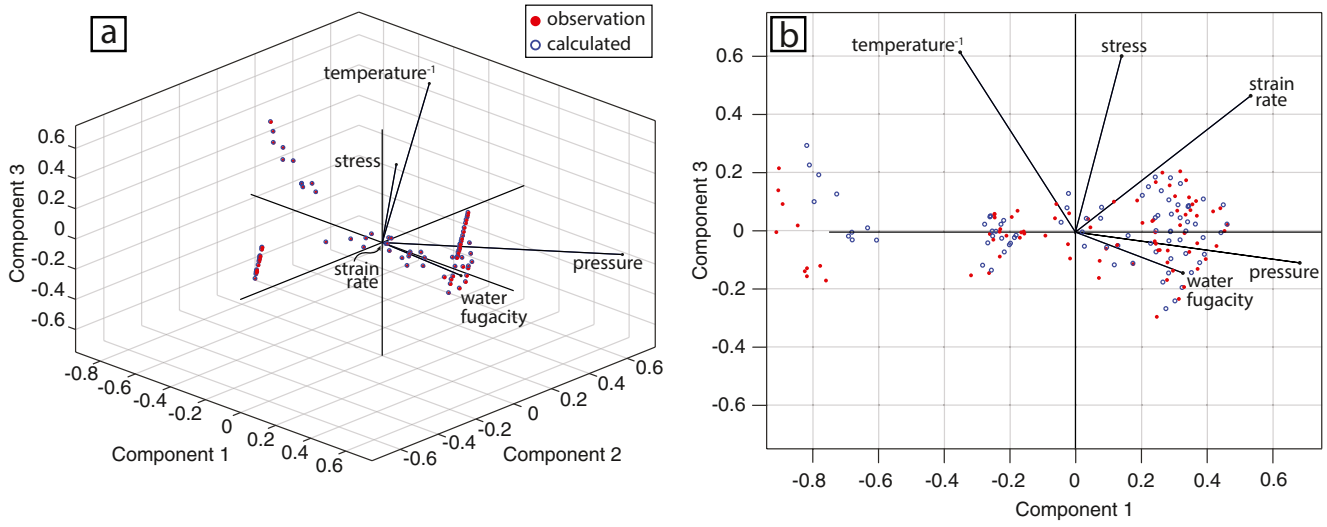

Figure 9. 3D views of the observational data, and results calculated using the "high-pressure" flow law parameters, relative to the first three principal component axes. (a) The view looks straight down the strain rate axis and confirms that the difference between the observed and calculated results lies along this axis. (b) Same data and parameters as (a) but viewed directly down the Component 2 axis, looking at the Component 1–Component 3 plane, with the temperature and strain-rate axes at right angles to each other. The plot shows that the fit between the observed and calculated results within each cluster does not change significantly with temperature, whereas it does change with pressure.

do not vary as a function of temperature but do clearly vary as a function of pressure. This validates our separation of the full data set into high- and low-pressure bins and suggests that temperature is not the factor controlling the differences in n, in contrast to the suggestions of Tokle et al. (2019).

4.3. Evaluating Flow Laws by Comparing Predicted and Field-Based Strain Rates

Comparisons of strain rates calculated from published flow laws as a function of stress under constant pressure (P)–temperature (T) conditions are illustrated in Figure 10. Compared to published flow laws, the "low-pressure" constitutive relationships presented here predict faster strain rates for given deformation conditions. Aside from the "low-pressure" calibration presented here, the flow laws that most closely agree with the field-based data are those of Hirth et al. (2001) and Tokle et al. (2019), both of which also integrate natural deformation data in some way. However, both predict strain rates slower than the natural field-based constraints, sometimes by more than 1 order of magnitude. At low T and high stress conditions (Figures 10a and 10b), the "low-pressure" flow law is in excellent agreement with field-based strain rates from the SSZ and WMCC, whereas all other flow laws underestimate the strain rates generally by more than 1 order of magnitude. At moderate T, moderate stress conditions (Figure 10c) and high T, low stress conditions (Figures 10d and 10e), the "low-pressure" flow law accurately predicts field-based strain rates to within error, while other flow laws underestimate field-based strain rates.

As an independent check, we also compare flow law predictions to constraints from the RGD, data from which were not used in the calibration (Figure 10f). Deformation conditions in the RGD were estimated by Dunlap et al. (1997) and Hirth et al. (2001). Differential stress was recalculated using the Cross et al. (2017) piezometer based on recrystallized grain size measurements bracketed between 20 and 160 μm from Dunlap et al. (1997), corresponding to differential stress $16 \leq \sigma \leq 70$ MPa. Published estimates broadly fit the "low-pressure" flow law as well as flow laws from Hirth et al. (2001) and Tokle et al. (2019), although any increase in strain rate beyond 5×10^{-14} s^{-1} fits better with the "low-pressure" flow law presented here.

The "high-pressure" flow law predicts strain rates for high-pressure experimental data reasonably well, but when extrapolated to geological strain rates (e.g., 10^{-15} to 10^{-11} s^{-1}), it predicts strain rates faster than observed by up to ~3 orders of magnitude. The failed extrapolation to geological conditions exemplifies two important points. (1) Although experiments from individual studies may be internally consistent, use of compiled experimental data may be prone to inconsistencies that arise from different experimental practices, including data interpretation and sample preparation. Another issue can arise from compiling data and calculating "global fit" parameters, in contrast to using the results of individual sets of experiments (Hirth & Kohlstedt, 2015). However, examination of individual high-pressure data sets in Figure 1c reveals that even when taken alone, none of them suggest $n > 2$, indicating this is likely not a significant issue in the strict sense as defined by Hirth and Kohlstedt (2015). (2) Because of the point made in (1), if experimental studies are to be applied accurately to geological conditions, it is critical to have constraints at slower strain rates and lower temperatures, pressures, and stresses, as even small errors in flow law parameters can cause large discrepancies when extrapolated over several orders of magnitude.

4.4. Further Investigating Differences in the *Effective* Stress Exponent

Our estimated value for the "low-pressure" data set of $n_{LP} = 3.5 \pm 0.2$ is higher than the theoretical stress sensitivity of $n = 3$ and somewhat less than the commonly cited value of $n \approx 4$ (Table 1). For the "high-pressure" data set, however, $n_{HP} = 2.0 \pm 0.1$ is significantly lower than the theoretical value for dislocation creep but agrees well with many experimental studies that calculate values in the range of $1.7 < n < 2.9$ (Table 1). Stress exponents that differ from $n = 3$ are commonly explained by the activity of deformation processes in addition to dislocation creep that result in a higher or lower *effective* stress exponent, n_{eff}. In the section below, we further explore the possible causes for the difference in n compared to previous studies and theoretical considerations.

Tokle et al. (2019) observed, as we do, that some of the experimental data are best fit by a stress exponent of $n \approx 4$, whereas other data are fit better by $n \leq 3$. They attributed the difference in the stress exponent to the activation of different rate-limiting slip systems in response to changes in temperature and stress: experiments conducted at >900°C and low stresses fit the higher exponent, and those conducted at lower

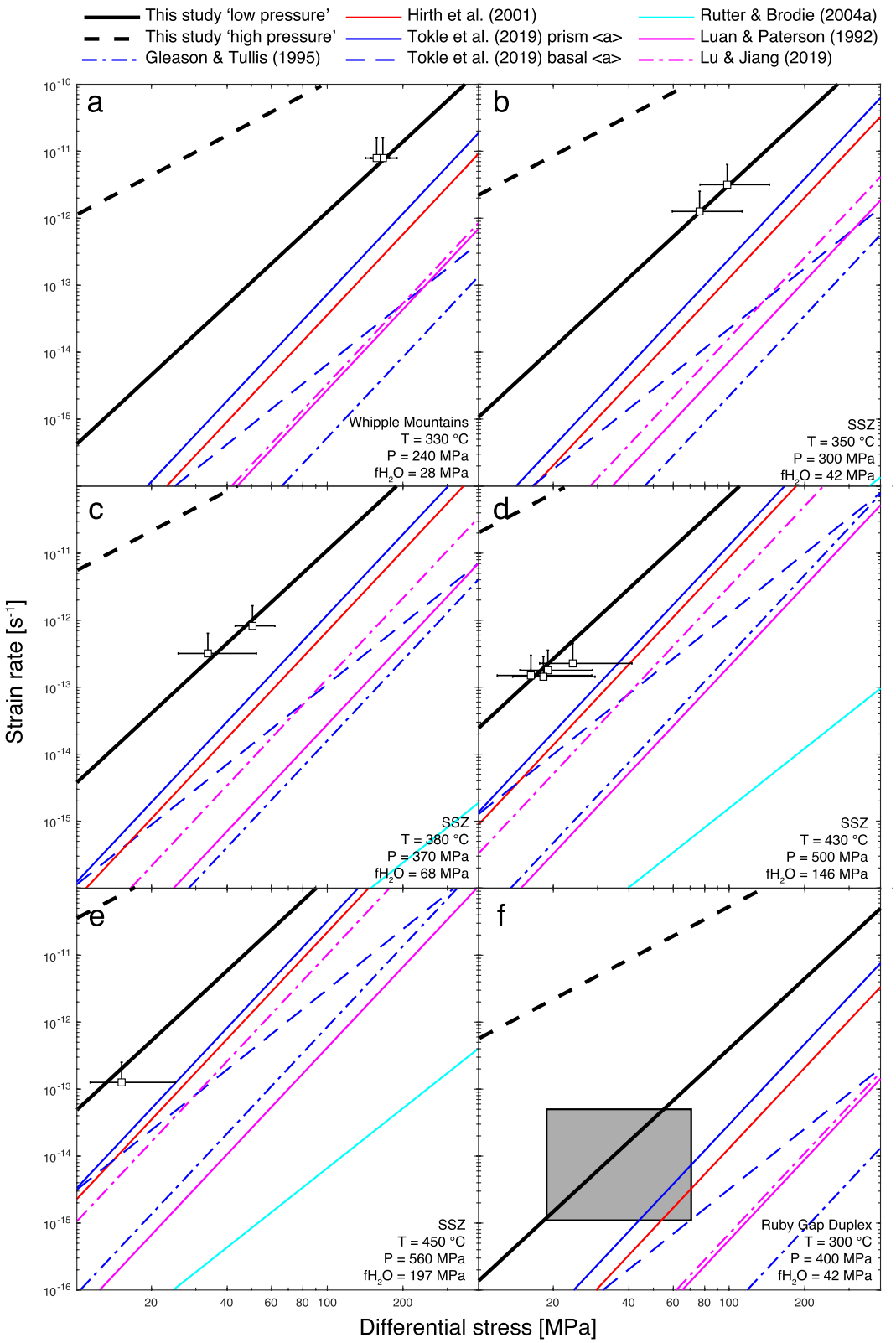
This study 'low pressure'
This study 'high pressure'
Gleason & Tullis (1995)
Hirth et al. (2001)
Tokle et al. (2019) prism <a>
Tokle et al. (2019) basal <a>
Rutter & Brodie (2004a)
Luan & Paterson (1992)
Lu & Jiang (2019)
a
Whipple Mountains
T = 330 °C
P = 240 MPa
fH2O = 28 MPa
b
SSZ
T = 350 °C
P = 300 MPa
fH2O = 42 MPa
c
SSZ
T = 380 °C
P = 370 MPa
fH2O = 68 MPa
d
SSZ
T = 430 °C
P = 500 MPa
fH2O = 146 MPa
e
SSZ
T = 450 °C
P = 560 MPa
fH2O = 197 MPa
f
Ruby Gap Duplex
T = 300 °C
P = 400 MPa
fH2O = 42 MPa
Strain rate [s-1]
Differential stress [MPa]

temperature and higher stresses fit the lower exponent. Data from Lusk and Platt (2020) used in this study, however, record *c*-axis CPOs indicative of slip on the basal <a>, ±rhomb <a>, and prism <a> systems, and a combination thereof, yet all samples plot closely along a line with a constant slope (Figure 6a). This suggests that the difference in n is not simply related to the active slip systems. It has been shown that CPO topology and intensity can reflect several variables, including temperature, finite strain, strain geometry, and water content, and CPOs can also record strong inheritance, especially in naturally deformed rocks (Heilbronner & Tullis, 2006; Law, 2014; Schmid & Casey, 1986; Stipp et al., 2002; Toy et al., 2008).

The problem that both studies encounter is that most of the higher temperature experiments are performed in a Paterson-type apparatus, in which the confining pressure is limited to 300 MPa, whereas the lower temperature experiments were conducted in Griggs-type apparatus at pressures generally around 1,500 MPa. As a result, it is not immediately clear whether pressure or temperature is the factor controlling the difference in exponent. Tokle et al. (2019) concluded that temperature is the controlling factor, based on a handful of experiments by Gleason and Tullis (1995) and Richter et al. (2016, 2018) conducted at high pressure and high temperature that are best fit by the higher exponent (Tokle et al., 2019, Figure 1e). Our conclusion that pressure is the controlling factor is based on (1) the clear distinction between the slopes of the high- and low-pressure data in $\log(\dot{\varepsilon})$–$\log(\sigma)$ space (our Figures 1c and Tokle et al., 2019, Figure 1a), (2) the fact that the pressure difference under discussion is very large (300 MPa vs. 700–1,600 MPa), whereas the temperature difference is rather modest (800°C–900°C vs. 927°C–1,200°C); (3) the fact that the field-based data, which are low T, fit the higher stress exponent, and (4) the results of our PCA, which demonstrate that temperature by itself does not affect the fit of the flow laws to the data (our Figure 9b), whereas pressure most definitely does.

4.4.1. Multiple Active Deformation Mechanisms

The above analysis is predicated on the assumption that the deformation mechanism for all natural and experimental samples is dislocation creep in quartz. In reality, there are likely multiple active deformation mechanisms, with the dominant one being that which produces the highest strain rate. The lower stress exponent in experiments conducted at higher confining pressure likely indicates that deformation mechanism(s) in addition to dislocation creep are active and that the combination of deformation mechanisms results in a lower *effective* stress exponent. These could include GSS mechanisms such as grain boundary sliding (GBS) or diffusion creep (e.g., Nabarro–Herring creep, Coble creep, or pressure solution).

One possibility is that in experiments yielding a lower stress exponent, strain was accommodated by GBS, or GBS in conjunction with dislocation creep (i.e., DisGBS; Hirth & Kohlstedt, 1995), which has been shown to have a stress sensitivity of $n = 2$ (Kohlstedt & Hansen, 2015). Direct evidence for GBS can be difficult to identify based solely on observation of the rock microstructure; for example, it is generally thought that GBS will produce weak CPOs, yet there is evidence suggesting the contrary (e.g., Hansen et al., 2011). However, not all high-pressure experiments produced fine-grained aggregates that would facilitate GBS, and it is unclear why GBS would be favored by higher confining pressures.

A second plausible explanation is an increased component of diffusion creep, specifically by pressure solution. Flow laws for deformation by pressure solution have a linear dependence on differential stress ($n = 1$) and a power law dependence for grain size (i.e., $m = 1$–3; den Brok, 1998; Paterson, 1995; Rutter, 1976; Rutter & Brodie, 2004a). The molality of aqueous SiO_2 increases with increasing pressure (Manning, 1994), which could make pressure solution a more effective process at accommodating strain in higher pressure rocks, especially those that are water saturated. Pressure solution and other diffusional creep mechanisms

Figure 10. A comparison between predicted and naturally constrained strain rates as a function of differential stress at deformation conditions calculated from Lusk and Platt (2020), Behr and Platt (2011), Dunlap et al. (1997), and Hirth et al. (2001). A qualitative check on flow law accuracy in reproducing strain rates of naturally deformed rocks is possible by comparing strain rates in iso-*P*–*T* plots to corresponding natural samples. Low (a, b), moderate (c), and high (d, e) *P*–*T* conditions from the SSZ and WMCC are plotted. Also included are deformation conditions from the RGD, indicated by the gray box in (f). Stresses in the RGD are from measurements of grain size ranging from 20 to 160 μm by Dunlap et al. (1997) using the Cross et al. (2017) calibration. *P*–*T* conditions and strain rates are from Dunlap et al. (1997) and Hirth et al. (2001). In the RGD, the "low-pressure" calibration as well as calibrations from Hirth et al. (2001) and Tokle et al. (2019) fit within error. All error bars on natural strain rates are one-sided as calculated values are minimum estimates. SSZ, Scandian shear zone; WMCC, Whipple Mountains metamorphic core complex; RGD, Ruby Gap Duplex.

are likely active over a wide range of deformation conditions (Cox & Paterson, 1991; Wheeler, 1992), although it may be difficult to find direct evidence for them, especially in mono-phase quartz aggregates, and at higher temperatures where additional deformation mechanisms are also active.

If both dislocation creep and a form of GSS creep (e.g., pressure solution, GBS) are active, the resulting *effective* stress exponent reflects the value of each individual stress exponent and the relative activity of each process. So long as both processes can act simultaneously without interference, the effect of GSS creep operating together with dislocation creep can be expressed as

$$\dot{\varepsilon}_{\text{composite}} = \dot{\varepsilon}_{\text{disl}} + \dot{\varepsilon}_{\text{GSS}} \tag{7}$$

which can be rewritten to an equivalent expression:

$$\dot{\varepsilon}_{\text{composite}} = A_{\text{disl}}\sigma^{n_{\text{disl}}} + A_{\text{GSS}}\sigma^{n_{\text{GSS}}} \tag{8}$$

where A_{disl} and A_{GSS} comprise terms for material properties, temperature, water fugacity, grain size, etc. n_{disl} is generally in the range of 2–4 (Table 1) and n_{GSS} is around 1 for diffusion creep (den Brok, 1998; Paterson, 1995; Rutter, 1976; Rutter & Brodie, 2004a) but may be higher for dynamic recrystallization-assisted dislocation creep (DRX creep; Platt & Behr, 2011) or DisGBS (Hirth & Kohlstedt, 1995), both of which are GSS. At constant P–T conditions in steady state, A_{disl} and A_{GSS} can be treated as constants and $\dot{\varepsilon}_{\text{composite}}$ is then a function of stress raised to a composite $n_{\text{effective}}$ which is a combination of the individual components, n_{disl} and n_{GSS}. The resulting apparent stress sensitivity will be a function of the relative proportions of each independent deformation mechanism, following the relationship below from Huet et al. (2014):

$$n_{\text{effective}} = \frac{\sum_i \phi_i a_i n_i}{\sum_i \phi_i a_i} \tag{9}$$

where ϕ_i is the relative contribution of the ith deformation mechanism, n_i is the stress sensitivity exponent, and a_i is the relationship between different values of n given by

$$a_i = \prod_{j \neq i} \left(n_j + 1\right) \tag{10}$$

To exemplify this relationship, equal parts of dislocation creep (assuming $n = 3$) and diffusion creep ($n = 1$) yield $n_{\text{effective}} = 2$. We therefore tentatively suggest that the low value of n determined for the high-pressure experimental data results from a component of GSS creep with a low value of n, in addition to dislocation creep. The proportion of GSS creep increases with pressure, which suggests that it may be pressure solution creep with a rate that is enhanced by increasing pressure.

If GSS creep is active in addition to dislocation creep *and* the grain size is controlled by the piezometric relationship, we can make an independent prediction of $n_{\text{effective}}$ to compare against our calculated value of $n_{\text{HP}} = 2.0 \pm 0.1$. The dynamically recrystallized grain size, d, can be related to the differential stress by the following empirically derived relationship:

$$d = K\sigma^{p} \tag{11}$$

where K is the piezometric constant, σ is differential stress, and p is the piezometric exponent. Combining Equations 1 and 11, the differential stress is also dependent on the piezometric exponent and grain size exponent such that $n^* = n–pm$ (Platt & Behr, 2011). Given a value of $p = -1.41 \pm 0.21$ (Cross et al., 2017), m = 1–3 for GSS creep (den Brok, 1998; Paterson, 1995; Rutter, 1976; Rutter & Brodie, 2004a), and $n = 3.5$ (from the low-pressure experiments and consistent with theoretical determinations), n^* ranges from 4.9 to 7.7. This range of values is not close to the calculated value of $n_{\text{HP}} = 2.0 \pm 0.1$, suggesting that these parameters are inconsistent with grain size following a piezometric relationship.

This observation emphasizes the importance of rock deformation experiments reaching a microstructural steady state, at which point continued strain no longer alters the physical microstructure (e.g., size, shape,

orientation of grains within the sample) if other extensive variables are held constant. The relatively low finite strains achieved in many rock deformation experiments (especially those performed in axial compression) and some experimentally produced rock microstructures casts doubt on whether experiments reach a microstructural steady state. In many such cases, continued strain would further alter the rock microstructure, likely entailing more extensive dynamic recrystallization in response to increased buildup of dislocations, leading to a uniform grain size reflecting the conditions of deformation (Heilbronner & Tullis, 2006). In experiments with a coarse and uniform initial grain size, the effect on the microstructure would be to decrease the mean grain size through dynamic recrystallization, which could lead to increased activity of GSS creep processes. In rocks with a spectrum of grain sizes, the effect may be to homogenize the stable grain size through a combination of dynamic recrystallization, grain growth, and/or grain consumption (Platt & Behr, 2011). Potential consequence of relatively low strain experiments not reaching a microstructural steady state is that the starting grain size may affect calculated rheological parameters through activation of additional deformation mechanisms, and the measured grain size(s) may not follow a piezometric relationship. For example, some experiments (e.g., Richter et al., 2016, 2018) use quartz aggregates characterized by a range of grain sizes within the same sample. In their experiments, Richter et al. (2018) observed that smaller diameter grain fractions deformed by a larger component of GSS creep compared to the larger grain fractions, which were interpreted to deform primarily by dislocation creep. These experiments produced a stress exponent of $n = 1.8–2.0$, similar to what we have calculated for the high-pressure data set.

5. Conclusions

Using MCMC analyses on natural and experimental data from similar confining pressures, we arrive at data set-consistent flow laws for dislocation creep in wet quartz aggregates. Integration of experimental data with natural observations greatly increases the range of strain rates, temperatures, and stresses at which quartz was deformed, resulting in flow law parameters that are constrained by, instead of extrapolated to, geological conditions. For conditions present in the middle crust where quartz controls rock rheology, flow law parameters for the "low-pressure" calibration are $\log(A) = -9.30 \pm 0.66$ MPa^{-n-r} s^{-1}, $r = 0.49 \pm 0.13$, $n = 3.5 \pm 0.2$, $Q = 118 \pm 5$ kJ mol^{-1}, and $V = 2.59 \pm 2.45$ cm^3 mol^{-1}. For the "high-pressure" calibration, we arrive at a different set of parameters: $\log(A) = -7.90 \pm 0.34$ MPa^{-n-r} s^{-1}, $r = 0.49 \pm 0.13$, $n = 2.0 \pm 0.1$, $Q = 77 \pm 8$ kJ mol^{-1}, and $V = 2.59 \pm 2.45$ cm^3 mol^{-1}. The "low-pressure" calibration fits best with field-based constraints and we therefore recommend these parameters for applications addressing the rheology of quartz-rich rocks at greenschist facies conditions. The transition between constitutive parameters based on confining pressure appears to be gradational (Figure 9), and the cutoff pressure used in this study only reflects data availability.

As demonstrated in this study, care should be taken in applying flow laws, especially those calibrated solely from experimental data, to naturally deformed rocks. This is evident in the effect of confining pressure and active deformation mechanism(s) on calculated flow law parameters, neither of which are fully resolved. At higher confining pressures, a low value of n may be the result of active deformation mechanism(s) in addition to dislocation creep, namely a GSS process (e.g., GBS or diffusion creep). Further work is needed to better understand the effects of deformation conditions on the stress sensitivity and other flow law parameters before experimental work alone can reliably be scaled to geological conditions.

Appendix A: Selection of Experimental Data

Below we outline the parameters used to filter experimental mechanical data included in this study:

1. The dominant deformation mechanism must be dislocation creep in quartz. Because of the conditions at which some experiments are conducted (e.g., high stress) and starting materials used (e.g., ultrafine-grained quartz) other deformation mechanisms may be active. These include brittle or semibrittle creep, GSS creep including solution–reprecipitation creep, and in some cases a clear component of GBS. Experimental runs that show clear evidence for brittle or semibrittle processes are excluded as these are generally easy to identify. Both natural and experimental samples likely include variable components of GSS creep, which can be difficult to quantify. Because not all studies explicitly comment on activity of GSS deformation mechanisms, and because GSS creep mechanisms are almost certainly active in natural

samples, we do not exclude data based on GSS creep. GSS creep is further addressed in the discussion. Any experiments that had measured stresses greater than the confining pressure are excluded due to the likelihood of semibrittle flow (Hirth & Tullis, 1994; Richter et al., 2018).

2. Because experimental data are integrated with constraints from naturally deformed rocks, experimental data are only included if they were performed on "wet quartz," that is quartz aggregates that include at least 0.1–0.4 wt.% H_2O, following Tokle et al. (2019). These conditions correspond to observations on the naturally deformed rocks used in this study, which we infer are water saturated. Furthermore, only including wet quartz deformation experiments validates the assumption that samples are water saturated (we assume a water activity, $a_{H_2O} = 1$), and water fugacity, f_{H_2O}, can therefore be calculated based on the pressure and temperature conditions of deformation.
3. Experiments must be conducted on quartz aggregates. The behavior of quartz single crystals has been shown to differ from that of aggregates (Holyoke & Kronenberg, 2013; Muto et al., 2011) making much of the work on single crystals not directly applicable to most geological conditions. Experiments must be conducted on pure α or β quartz of natural or synthetic origin. There are no apparent resolvable effects of the α–β transition on quartz rheology and therefore data from both stability fields are included for this analysis (Tokle et al., 2019, Figure 1b; but see Fukuda & Shimizu, 2017, for an opposing viewpoint). Experiments in which secondary phases or other quartz polymorphs (e.g., coesite–reported in Richter et al., 2016, 2018) are present are not included. Experiments on gel-origin samples (Luan & Paterson, 1992; Nachlas & Hirth, 2015; Paterson & Luan, 1990), which are reported as relatively impure, and on sintered quartz (Luan & Paterson, 1992; Paterson & Luan, 1990), which the authors suggest were not equilibrated with respect to water and disregarded, were not included in this study. A hot-pressing process was also used by Rutter and Brodie (2004b) and Fukuda et al. (2018) but they confirmed high water contents of 0.6% and 0.25%, respectively. Additionally, the high confining pressures of Fukuda et al. (2018) may facilitate faster water equilibration (Luan & Paterson, 1992, and references therein).
4. Experiments must have reached mechanical steady state. Experiments in which total strains are below the threshold for mechanical steady state, or the deforming material exhibits significant strain weakening or strain hardening behavior, are excluded. Where possible, stresses are measured from the portion of the stress–strain curve that is flat and at high strain (i.e., in mechanical steady state).
5. Experiments that show evidence for inclusion of melt (e.g., Gleason & Tullis, 1995; Koch et al., 1989; Luan & Paterson, 1992) are disregarded in this analysis, as the effect of melt–mineral interaction on rock rheology adds an additional complication, which is beyond the scope of this study.

Data Availability Statement

Data presented in this study are compiled from the literature and are available through Behr and Platt (2011), Chernak et al. (2009), Fukuda et al. (2018), Gleason and Tullis (1995), Heilbronner and Tullis (2002, 2006), Hirth and Tullis (1992), Holyoke and Kronenberg (2013), Holyoke and Tullis (2006), Kidder et al. (2016), Koch et al. (1989), Kronenberg and Tullis (1984), Luan and Paterson (1992), Lusk and Platt (2020), Palazzin et al. (2018), Post et al. (1996), Richter et al. (2016, 2018), Rutter and Brodie (2004b), Stipp and Tullis (2003), Stipp et al. (2006), and Tullis and Wenk (1994). Our complete data set is provided as a supplemental table (Table S1), which includes reference to each data source.

Acknowledgments
We would like to thank Holger Stünitz and Greg Hirth for insightful and constructive reviews that greatly improved the content and clarity of this manuscript. We also thank George Rossman and Andreas Kronenberg for advice about water weakening processes. This research was funded by NSF EAR-1650173 awarded to John P. Platt. Alexander D. Lusk would like to acknowledge funding from a College Doctoral Fellowship at the University of Southern California.

References

Behr, W. M., & Platt, J. P. (2011). A naturally constrained stress profile through the middle crust in an extensional terrane. *Earth and Planetary Science Letters*, *303*(3–4), 181–192. https://doi.org/10.1016/j.epsl.2010.11.044

Boutonnet, E., Leloup, P. H., Sassier, C., Gardien, V., & Ricard, Y. (2013). Ductile strain rate measurements document long-term strain localization in the continental crust. *Geology*, *41*, 819–822. https://doi.org/10.1130/G33723.1

Brace, W. F., & Kohlstedt, D. L. (1980). Limits on lithospheric stress imposed by laboratory experiments. *Journal of Geophysical Research*, *85*, 6248–6252. https://doi.org/10.1029/JB085iB11p06248

Chernak, L. J., Hirth, G., Selverstone, J., & Tullis, J. (2009). Effect of aqueous and carbonic fluids on the dislocation creep strength of quartz. *Journal of Geophysical Research*, *114*, B04201. https://doi.org/10.1029/2008JB005884

Cox, S. F., & Paterson, M. S. (1991). Experimental dissolution–precipitation creep in quartz aggregates at high temperatures. *Geophysical Research Letters*, *18*, 1401–1404. https://doi.org/10.1029/91GL01802

Cross, A. J., Prior, D. J., Stipp, M., & Kidder, S. (2017). The recrystallized grain size piezometer for quartz: An EBSD-based calibration. *Geophysical Research Letters*, *44*, 6667–6674. https://doi.org/10.1002/2017GL073836

den Brok, S. W. J. (1998). Effect of microcracking on pressure–solution strain rate: The Gratz grain-boundary model. *Geology*, *26*, 915–918.

Dixon, N. A., & Durham, W. B. (2018). Measurement of activation volume for creep of dry olivine at upper-mantle conditions. *Journal of Geophysical Research: Solid Earth*, *123*, 8459–8473. https://doi.org/10.1029/2018JB015853

Dunlap, W. J., Hirth, G., & Teyssier, C. (1997). Thermomechanical evolution of a ductile duplex. *Tectonics*, *16*(6), 983–1000. https://doi.org/10.1029/97TC00614

Foreman-Mackey, D. (2016). corner.py: Scatterplot matrices in Python. *Journal of Open Source Software*, *1*(2), 24. https://doi.org/10.21105/joss.00024

Fukuda, J.-I., Holyoke, C. W., III, & Kronenberg, A. K. (2018). Deformation of fine-grained quartz aggregates by mixed diffusion and dislocation creep. *Journal of Geophysical Research: Solid Earth*, *123*, 4676–4696. https://doi.org/10.1029/2017JB015133

Fukuda, J.-I., & Shimizu, I. (2017). Theoretical derivation of flow laws for quartz dislocation creep: Comparisons with experimental creep data and extrapolation to natural conditions using water fugacity corrections. *Journal of Geophysical Research: Solid Earth*, *122*, 5956–5971. https://doi.org/10.1002/2016JB013798

Gleason, G. C., & Tullis, J. (1993). Improving flow laws and piezometers for quartz and feldspar aggregates. *Geophysical Research Letters*, *20*, 2111–2114. https://doi.org/10.1029/93GL02236

Gleason, G. C., & Tullis, J. (1995). A flow law for dislocation creep of quartz aggregates determined with the molten salt cell. *Tectonophysics*, *247*, 1–23. https://doi.org/10.1016/0040-1951(95)00011-B

Griggs, D. T., & Blacic, J. D. (1965). Quartz: Anomalous weakness of synthetic crystals. *Science*, *147*, 292–295.

Hansen, L. N., Zimmerman, M. E., & Kohlstedt, D. L. (2011). Grain boundary sliding in San Carlos olivine: Flow law parameters and crystallographic-preferred orientation. *Journal of Geophysical Research*, *116*, B08201. https://doi.org/10.1029/2011JB008220

Heilbronner, R., & Tullis, J. (2002). The effect of static annealing on microstructures and crystallographic preferred orientations of quartzites experimentally deformed in axial compression and shear. *Geological Society, London, Special Publications*, *200*, 191–218. https://doi.org/10.1144/GSL.SP.2001.200.01.12

Heilbronner, R., & Tullis, J. (2006). Evolution of *c* axis pole figures and grain size during dynamic recrystallization: Results from experimentally sheared quartzite. *Journal of Geophysical Research*, *111*, B10202. https://doi.org/10.1029/2005JB004194

Hirth, G., & Beeler, N. M. (2015). The role of fluid pressure on frictional behavior at the base of the seismogenic zone. *Geology*, *43*(3), 223–226. https://doi.org/10.1130/G36361.1

Hirth, G., & Kohlstedt, D. L. (1995). Experimental constraints on the dynamics of the partially molten upper mantle: Deformation in the diffusion creep regime. *Journal of Geophysical Research*, *100*, 1981–2001. https://doi.org/10.1029/94JB02128

Hirth, G., & Kohlstedt, D. L. (2015). The stress dependence of olivine creep rate: Implications for extrapolation of lab data and interpretation of recrystallized grain size. *Earth and Planetary Science Letters*, *418*, 20–26. https://doi.org/10.1016/j.epsl.2015.02.013

Hirth, G., Teyssier, C., & Dunlap, J. W. (2001). An evaluation of quartzite flow laws based on comparisons between experimentally and naturally deformed rocks. *International Journal of Earth Sciences*, *90*, 77–87. https://doi.org/10.1007/s005310000152

Hirth, G., & Tullis, J. (1992). Dislocation creep regimes in quartz aggregates. *Journal of Structural Geology*, *14*, 145–159. https://doi.org/10.1016/0191-8141(92)90053-Y

Hirth, G., & Tullis, J. (1994). The brittle–plastic transition in experimentally deformed quartz aggregates. *Journal of Geophysical Research*, *99*, 11731–11747. https://doi.org/10.1029/93JB02873

Holyoke, C. W., & Kronenberg, A. K. (2010). Accurate differential stress measurement using the molten salt cell and solid salt assemblies in the Griggs apparatus with applications to strength, piezometers and rheology. *Tectonophysics*, *494*, 17–31. https://doi.org/10.1016/j.tecto.2010.08.001

Holyoke, C. W., & Kronenberg, A. K. (2013). Reversible water weakening of quartz. *Earth and Planetary Science Letters*, *374*, 185–190. https://doi.org/10.1016/j.epsl.2013.05.039

Holyoke, C. W., & Tullis, J. (2006). Formation and maintenance of shear zones. *Geology*, *34*, 105–108. https://doi.org/10.1130/G22116.1

Huet, B., Yamato, P., & Grasemann, B. (2014). The Minimized Power Geometric model: An analytical mixing model for calculating polyphase rock viscosities consistent with experimental data. *Journal of Geophysical Research: Solid Earth*, *119*, 3897–3924. https://doi.org/10.1002/2013JB010453

Hughes, C. A., Jessup, M. J., Shaw, C. A., & Newell, D. L. (2019). Deformation conditions during syn-convergent extension along the Cordillera Blanca shear zone, Peru. *Geosphere*, *15*(4), 1342–1367. https://doi.org/10.1130/GES02040.1

Hughes, C. A., Jessup, M. J., Shaw, C. A., & Newell, D. L. (2020). Evidence for strain rate variation and an elevated transient geothermal gradient during shear zone evolution in the Cordillera Blanca, Peru. *Tectonophysics*, *794*, 228610. https://doi.org/10.1016/j.tecto.2020.228610

Karato, S.-I. (2008). *Deformation of earth materials. An introduction to the rheology of solid Earth* (Vol. 463). New York, NY: Cambridge University Press.

Karato, S.-I., & Jung, H. (2003). Effects of pressure on high-temperature dislocation creep in olivine. *Philosophical Magazine*, *83*, 401–414. https://doi.org/10.1080/0141861021000025829

Kidder, S., Avouac, J. P., & Chan, Y. C. (2012). Constraints from rocks in the Taiwan orogen on crustal stress levels and rheology. *Journal of Geophysical Research: Solid Earth*, *117*(B9). https://doi.org/10.1029/2012JB009303

Kidder, S., Hirth, G., Avouac, J.-P., & Behr, W. (2016). The influence of stress history on the grain size and microstructure of experimentally deformed quartzite. *Journal of Structural Geology*, *83*, 194–206. https://doi.org/10.1016/j.jsg.2015.12.004

Koch, P. S., Christie, J. M., Ord, A., & George, R. P. (1989). Effect of water on the rheology of experimentally deformed quartzite. *Journal of Geophysical Research*, *94*, 13975–13996. https://doi.org/10.1029/JB094iB10p13975

Kohlstedt, D. L., Evans, B., & Mackwell, S. J. (1995). Strength of the lithosphere: Constraints imposed by laboratory experiments. *Journal of Geophysical Research*, *100*, 17587–17602.

Kohlstedt, D. L., & Hansen, L. N. (2015). Constitutive Equations, Rheological Behavior, and Viscosity of Rocks. In S. Gerald (Ed.), *Treatise on Geophysics* (Vol. 2, ed. 2nd, pp. 441–472). Oxford: Elsevier.

Kronenberg, A. K. (1994). Chapter 4. Hydrogen speciation and chemical weakening of quartz. *Reviews in Mineralogy*, *29*, 123–176.

Kronenberg, A. K., & Tullis, J. (1984). Flow strengths of quartz aggregates: Grain size and pressure effects due to hydrolytic weakening. *Journal of Geophysical Research*, *89*, 4281–4297. https://doi.org/10.1029/JB089iB06p04281

Law, R. D. (2014). Deformation thermometry based on quartz *c*-axis fabrics and recrystallization microstructures: A review. *Journal of Structural Geology*, *66*, 129–161. https://doi.org/10.1016/j.jsg.2014.05.023

Lu, L. X., & Jiang, D. (2019). Quartz flow law revisited: The significance of pressure dependence of the activation enthalpy. *Journal of Geophysical Research: Solid Earth*, *124*, 241–256. https://doi.org/10.1029/2018JB016226

Luan, F. C., & Paterson, M. S. (1992). Preparation and deformation of synthetic aggregates of quartz. *Journal of Geophysical Research*, *97*, 301–320. https://doi.org/10.1029/91JB01748

Lusk, A. D. J., & Platt, J. P. (2020). The deep structure and rheology of a plate boundary-scale shear zone: Constraints from an exhumed Caledonian shear zone, NW Scotland. *Lithosphere*, *2020*, 1–33. https://doi.org/10.2113/2020/8824736

Manning, C. E. (1994). The solubility of quartz in H_2O in the lower crust and upper mantle. *Geochimica et Cosmochimica Acta*, *58*, 4831–4839. https://doi.org/10.1016/0016-7037(94)90214-3

Metropolis, N., Rosenbluth, A. W., Rosenbluth, M. N., Teller, A. H., & Teller, E. (1953). Equation of state calculations by fast computing machines. *The Journal of Chemical Physics*, *21*(6), 1087–1092. https://doi.org/10.1063/1.1699114

Muto, J., Hirth, G., Heilbronner, R., & Tullis, J. (2011). Plastic anisotropy and fabric evolution in sheared and recrystallized quartz single crystals. *Journal of Geophysical Research*, *116*, B02206. https://doi.org/10.1029/2010JB007891

Nachlas, W. O., & Hirth, G. (2015). Experimental constraints on the role of dynamic recrystallization on resetting the Ti-in-quartz thermobarometer. *Journal of Geophysical Research: Solid Earth*, *120*, 8120–8137. https://doi.org/10.1002/2015JB012274

Neal, R. M. (1995). *Bayesian learning for neural networks* (PhD thesis). Retrieved from University of Toronto (www.cs.utoronto.ca). Toronto, Ontario, Canada: Department of Computer Science, University of Toronto

Neal, R. M. (2011). MCMC using Hamiltonian dynamics. In S. Brooks, A. Gelman, G. Jones, & X.-L. Meng (Eds.), Handbook of Markov chain Monte Carlo (Ch. 5). Boca Raton, FL: Chapman & Hall/CRC.

Palazzin, G., Raimbourg, H., Stünitz, H., Heilbronner, R., Neufeld, K., & Précigout, J. (2018). Evolution in H_2O contents during deformation of polycrystalline quartz: An experimental study. *Journal of Structural Geology*, *114*, 95–110. https://doi.org/10.1016/j.jsg.2018.05.021

Paterson, M. S. (1987). Problems in the extrapolation of laboratory rheological data. *Tectonophysics*, *133*, 33–43. https://doi.org/10.1016/0040-1951(87)90278-2

Paterson, M. S. (1989). The interaction of water with quartz and its influence in dislocation flow—An overview. In S.-I. Karato & M. Toriumi (Eds.), *Rheology of solids and of the Earth* (pp. 107–142). Oxford: Oxford University Press.

Paterson, M. S. (1995). A theory for granular flow accommodated by material transfer via an intergranular fluid. *Tectonophysics*, *245*(3–4), 135–151. https://doi.org/10.1016/0040-1951(94)00231-W

Paterson, M. S., & Luan, F. C. (1990). Quartzite rheology under geological conditions. *Geological Society, London, Special Publications*, *54*, 299–307. https://doi.org/10.1144/GSL.SP.1990.054.01.26

Paterson, M. S., & Olgaard, D. L. (2000). Rock deformation tests to large shear strains in torsion. *Journal of Structural Geology*, *22*, 1341–1358. https://doi.org/10.1016/s0191-8141(00)00042-0

Pfiffner, O. A., & Ramsay, J. G. (1982). Constraints on geological strain rates: Arguments from finite strain states of naturally deformed rocks. *Journal of Geophysical Research*, *87*, 311–321. https://doi.org/10.1029/JB087iB01p00311

Platt, J. P., & Behr, W. M. (2011). Grainsize evolution in ductile shear zones: Implications for strain localization and the strength of the lithosphere. *Journal of Structural Geology*, *33*, 537–550. https://doi.org/10.1016/j.jsg.2011.01.018

Poirier, J. P. (1985). *Creep of crystals*. Cambridge, UK: Cambridge University Press. https://doi.org/10.1017/cbo9780511564451

Post, A. D., Tullis, J., & Yund, R. A. (1996). Effects of chemical environment on dislocation creep of quartzite. *Journal of Geophysical Research*, *101*, 22143–22155. https://doi.org/10.1029/96JB01926

Richter, B., Stünitz, H., & Heilbronner, R. (2016). Stresses and pressures at the quartz-to-coesite phase transformation in shear deformation experiments. *Journal of Geophysical Research: Solid Earth*, *121*, 8015–8033. https://doi.org/10.1002/2016JB013084

Richter, B., Stünitz, H., & Heilbronner, R. (2018). The brittle-to-viscous transition in polycrystalline quartz: An experimental study. *Journal of Structural Geology*, *114*, 1–21. https://doi.org/10.1016/j.jsg.2018.06.005

Rutter, E. H. (1976). A discussion on natural strain and geological structure—The kinetics of rock deformation by pressure solution. *Philosophical Transactions of the Royal Society of London - Series A: Mathematical and Physical Sciences*, *283*(1312), 203–219. https://doi.org/10.1098/rsta.1976.0079

Rutter, E. H., & Brodie, K. H. (2004a). Experimental grain size-sensitive flow of hot-pressed Brazilian quartz aggregates. *Journal of Structural Geology*, *26*(11), 2011–2023. https://doi.org/10.1016/j.jsg.2004.04.006

Rutter, E. H., & Brodie, K. H. (2004b). Experimental intracrystalline plastic flow in hot-pressed synthetic quartzite prepared from Brazilian quartz crystals. *Journal of Structural Geology*, *26*, 259–270. https://doi.org/10.1016/S0191-8141(03)00096-8

Rybacki, E., Gottschalk, M., Wirth, R., & Dresen, G. (2006). Influence of water fugacity and activation volume on the flow properties of fine-grained anorthite aggregates. *Journal of Geophysical Research*, *111*, B03203. https://doi.org/10.1029/2005JB003663

Salvatier, J., Wiecki, T. V., & Fonnesbeck, C. (2016). Probabilistic programming in Python using PyMC3. *PeerJ Computer Science*, *2*, e55. https://doi.org/10.7717/peerj-cs.55

Sassier, C., Leloup, P. H., Rubatto, D., Galland, O., Yue, Y., & Lin, D. (2009). Direct measurement of strain rates in ductile shear zones: A new method based on syntectonic dikes. *Journal of Geophysical Research*, *114*, B01406. https://doi.org/10.1029/2008JB005597

Schmid, S. M., & Casey, M. (1986). Complete fabric analysis of some commonly observed quartz *C*-axis patterns. *Radiated Energy and the Physics of Faulting*, *36*, 263–286. https://doi.org/10.1029/GM036p0263

Sterner, S. M., & Pitzer, K. S. (1994). An equation of state for carbon dioxide valid from zero to extreme pressures. *Contributions to Mineralogy and Petrology*, *117*, 362–374. https://doi.org/10.1007/bf00307271

Stipp, M., Stünitz, H., Heilbronner, R., & Schmid, S. M. (2002). The eastern Tonale fault zone: A 'natural laboratory' for crystal plastic deformation of quartz over a temperature range from 250 to 700°C. *Journal of Structural Geology*, *24*, 1861–1884. https://doi.org/10.1016/S0191-8141(02)00035-4

Stipp, M., & Tullis, J. (2003). The recrystallized grain size piezometer for quartz. *Geophysical Research Letters*, *30*(21), 2088. https://doi.org/10.1029/2003GL018444

Stipp, M., Tullis, J., & Behrens, H. (2006). Effect of water on the dislocation creep microstructure and flow stress of quartz and implications for the recrystallized grain size piezometer. *Journal of Geophysical Research*, *111*, B04201. https://doi.org/10.1029/2005JB003852

Takeshita, T. (1996). Estimate of physical conditions for deformation based on *c*-axis transitions in naturally deformed quartzite. *The Journal of the Geological Society of Japan*, *102*(3), 211–222.

Tokle, L., Hirth, G., & Behr, W. M. (2019). Flow laws and fabric transitions in wet quartzite. *Earth and Planetary Science Letters*, *505*, 152–161. https://doi.org/10.1016/j.epsl.2018.10.017

Toy, V. G., Prior, D. J., & Norris, R. J. (2008). Quartz fabrics in the Alpine Fault mylonites: Influence of pre-existing preferred orientations on fabric development during progressive uplift. *Journal of Structural Geology*, *30*(5), 602–621. https://doi.org/10.1016/j.jsg.2008.01.001

Tullis, J., & Wenk, H.-R. (1994). Effect of muscovite on the strength and lattice preferred orientations of experimentally deformed quartz aggregates. *Materials Science and Engineering: A*, *175*, 209–220. https://doi.org/10.1016/0921-5093(94)91060-X

Weertman, J. (1968). Dislocation climb theory of steady-state creep. *Transactions of American Society for Metals*, *61*, 681–694.

Wheeler, J. (1992). Importance of pressure solution and coble creep in the deformation of polymineralic rocks. *Journal of Geophysical Research*, *97*, 4579–4586. https://doi.org/10.1029/91JB02476